Electronic Supplementary Information for Dalton Transactions

Electronic Supplementary Information

for

A Convenient Ligand Exchange Pathway to [2Fe-2S] Ferredoxin Analogues

*Joachim Ballmann, Xianru Sun, Sebastian Dechert, Benjamin Schneider and Franc Meyer**

Institut für Anorganische Chemie, Georg-August-Universität,
Tammannstrasse 4, D-37077 Göttingen, Germany.

* To whom correspondence should be addressed: E-mail: franc.meyer@chemie.uni-goettingen.de; Phone: +49-551-39-3012; Fax: +49-551-39-3063.

Total pages: 39

Table of contents:

1. Electrospray ionization mass spectra

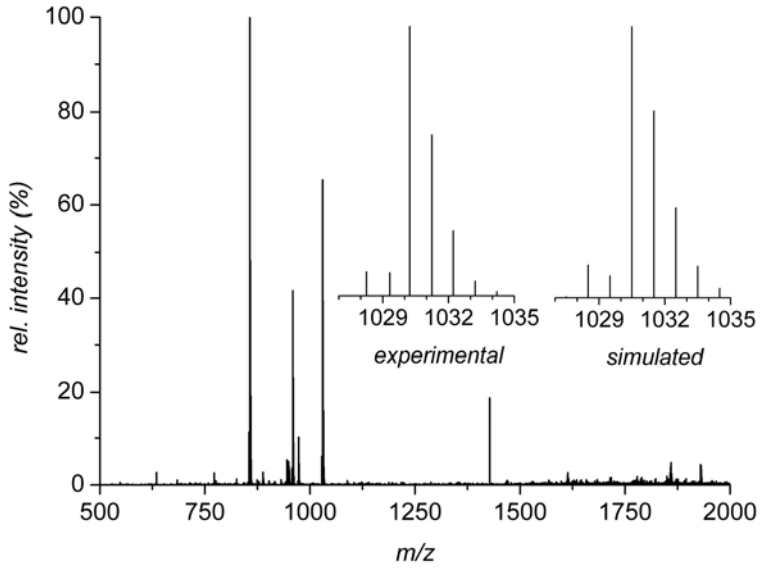

Figure S1: Positive ion ESI-MS spectrum of **2** in MeCN/DMF (10/1, v/v) solution. The insets show the experimental and expected isotopic distribution pattern for $[M + NEt_4]^+$.

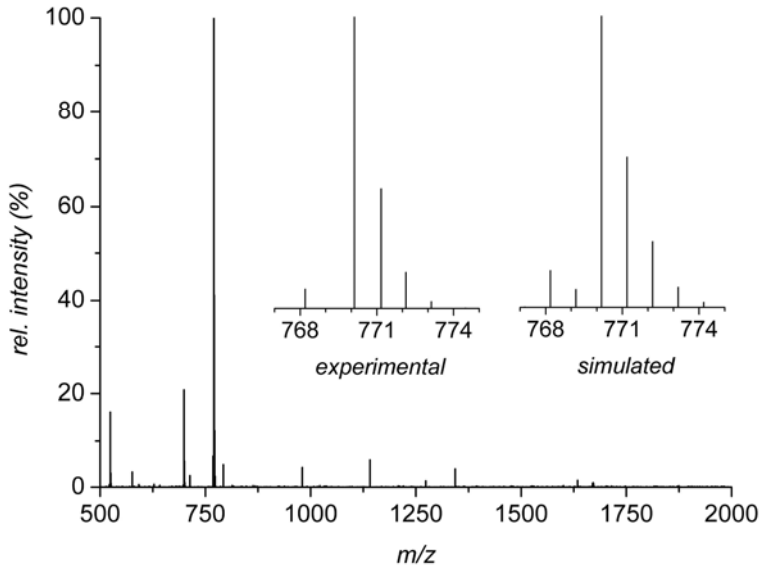

Figure S2: Negative ion ESI-MS spectrum of **2** in MeCN/ DMF (10/1, v/v) solution. The insets show the experimental and expected isotopic distribution pattern for $[M – NEt_4]^-$.

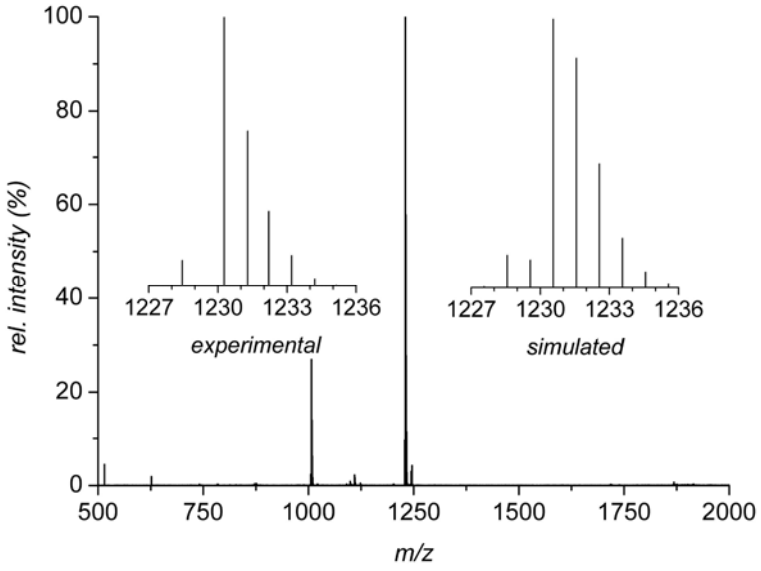

Figure S3: Positive ion ESI-MS spectrum of **3** in MeCN/ DMF (10/1, v/v) solution. The insets show the experimental and expected isotopic distribution pattern for $[M + NEt_4]^+$.

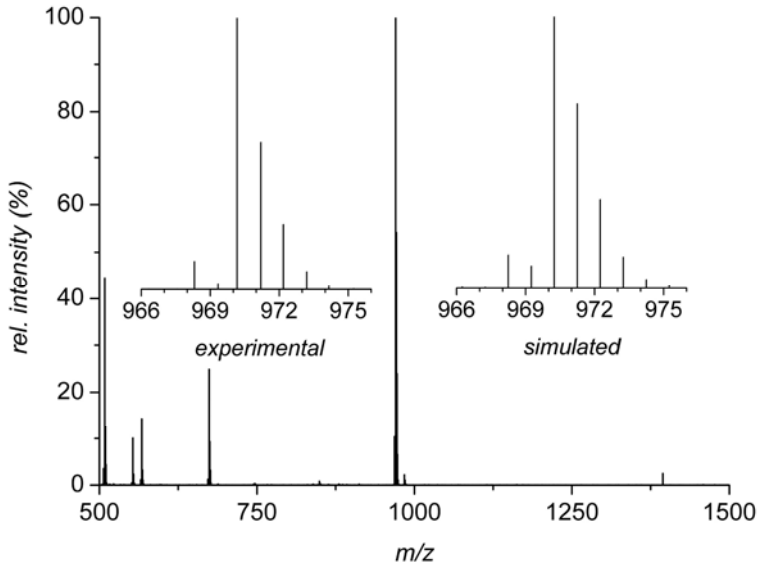

Figure S4: Negative ion ESI-MS spectrum of **3** in MeCN/ DMF (10/1, v/v) solution. The insets show the experimental and expected isotopic distribution pattern for $[M - NEt_4]^-$.

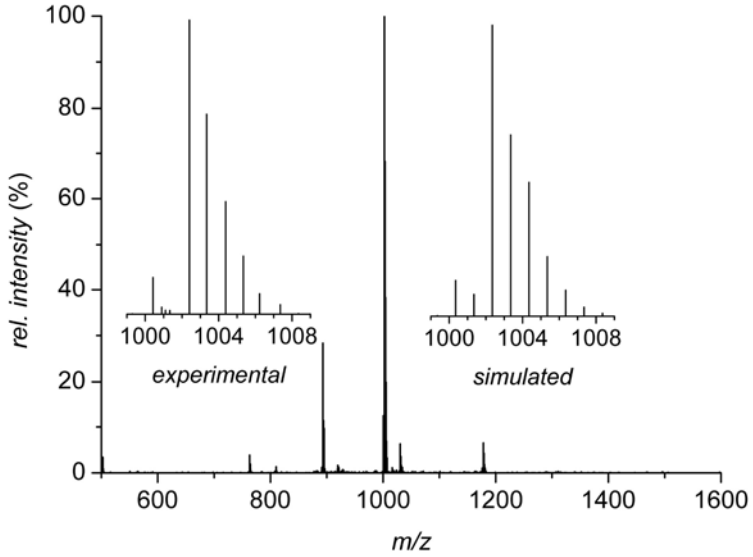

Figure S5: Positive ion ESI-MS spectrum of **4a** in MeCN solution. The insets show the experimental and expected isotopic distribution pattern for $[M + NEt_4]^+$.

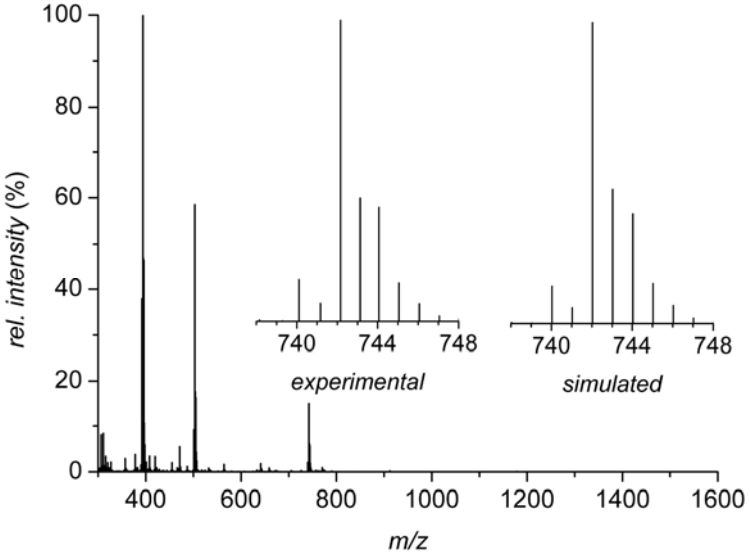

Figure S6: Negative ion ESI-MS spectrum of **4a** in MeCN solution. The insets show the experimental and expected isotopic distribution pattern for $[M - NEt_4]^-$.

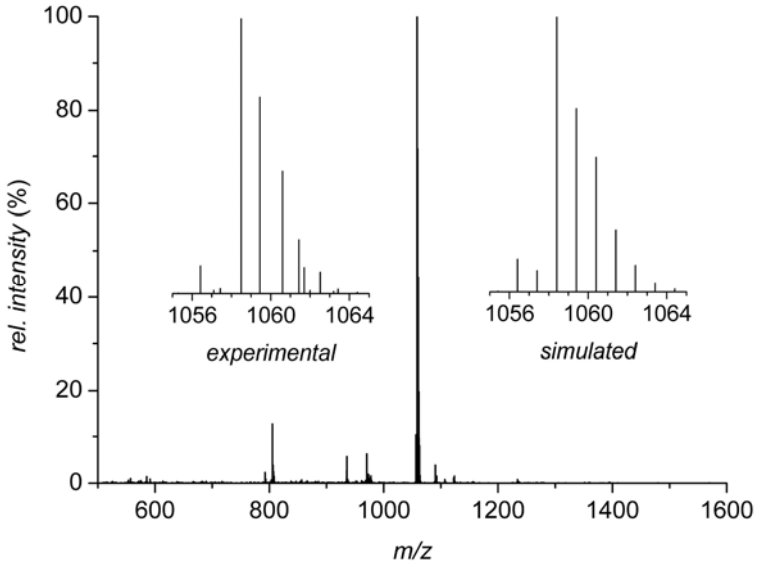

Figure S7: Positive ion ESI-MS spectrum of **4b** in MeCN solution. The insets show the experimental and expected isotopic distribution pattern for $[M + NEt_4]^+$.

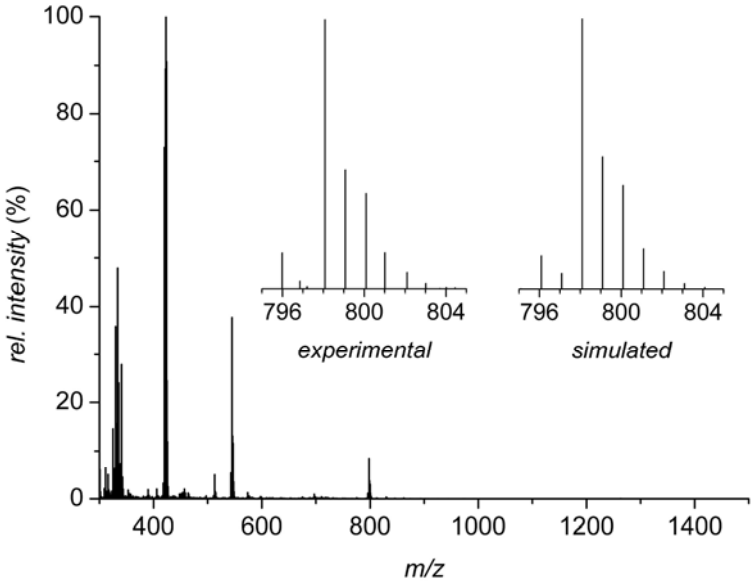

Figure S8: Negative ion ESI-MS spectrum of **4b** in MeCN solution. The insets show the experimental and expected isotopic distribution pattern for $[M – NEt_4]^-$.

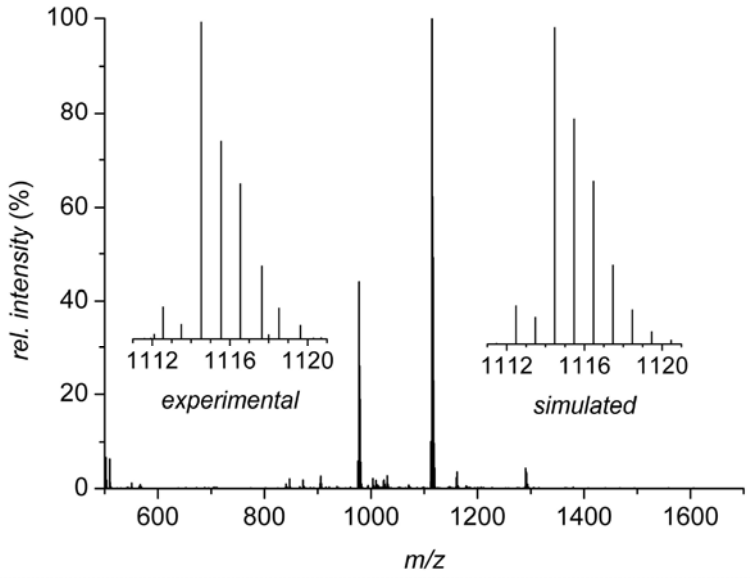

Figure S9: Positive ion ESI-MS spectrum of **4c** in MeCN solution. The insets show the experimental and expected isotopic distribution pattern for $[M + NEt_4]^+$.

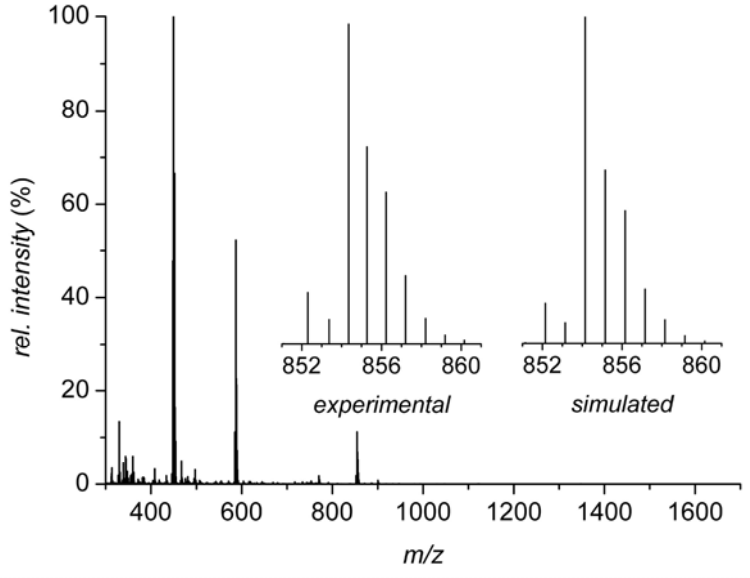

Figure S10: Negative ion ESI-MS spectrum of **4c** in MeCN solution. The insets show the experimental and expected isotopic distribution pattern for $[M - NEt_4]^-$.

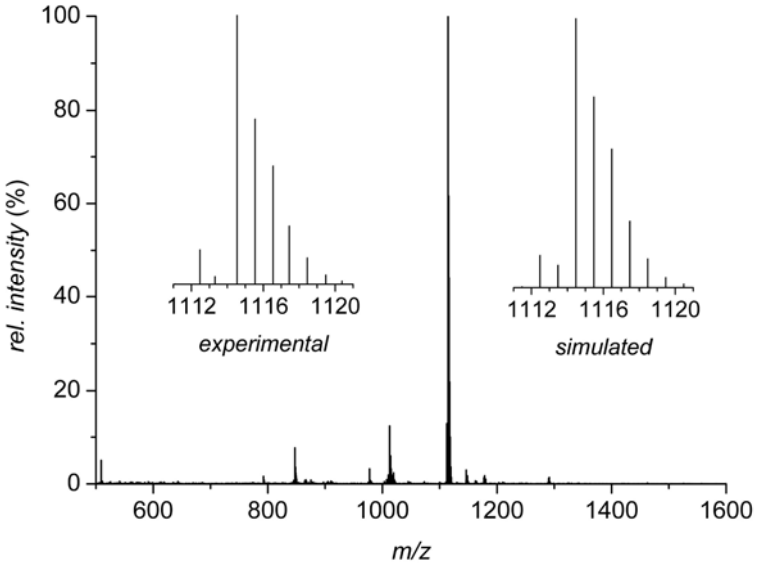

Figure S11: Positive ion ESI-MS spectrum of **4d** in MeCN solution. The insets show the experimental and expected isotopic distribution pattern for $[M + NEt_4]^+$.

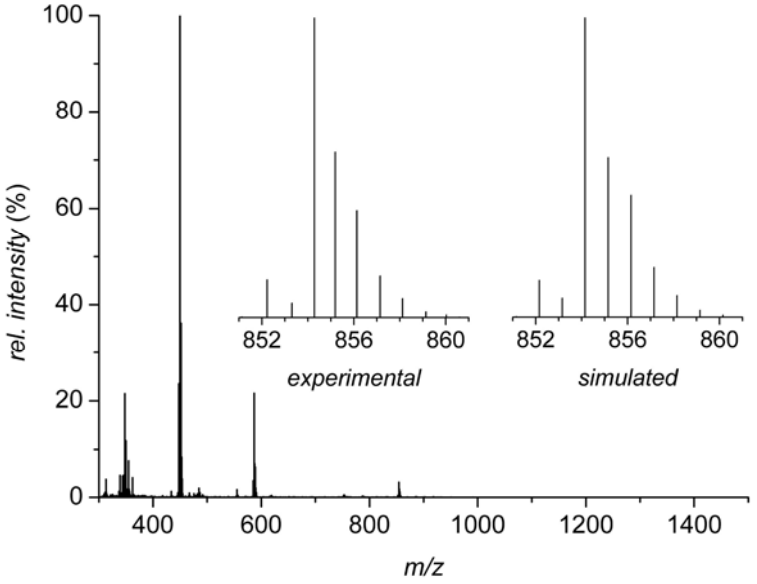

Figure S12: Negative ion ESI-MS spectrum of **4d** in MeCN solution. The insets show the experimental and expected isotopic distribution pattern for $[M – NEt_4]^-$.

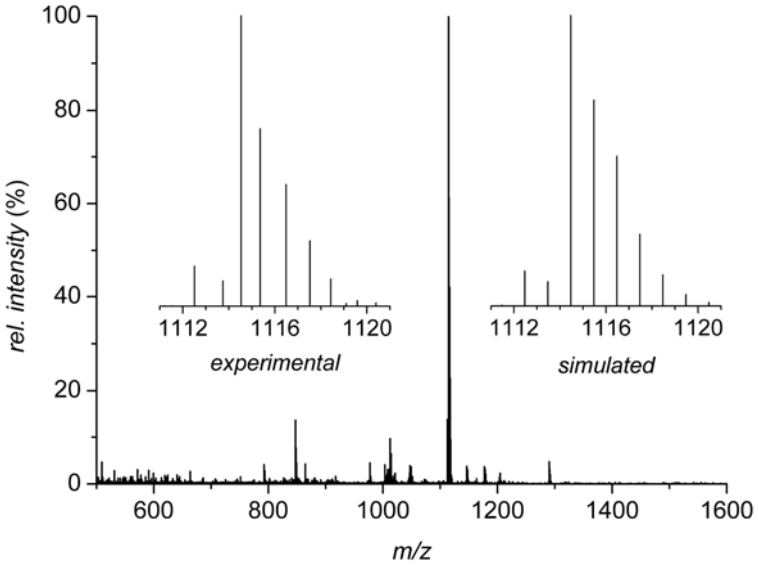

Figure S13: Positive ion ESI-MS spectrum of **4e** in MeCN solution. The insets show the experimental and expected isotopic distribution pattern for $[M + NEt_4]^+$.

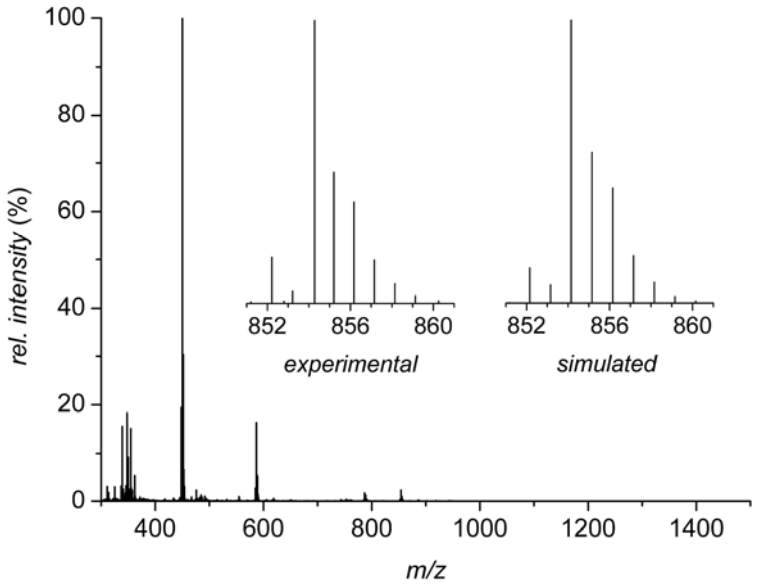

Figure S14: Negative ion ESI-MS spectrum of **4e** in MeCN solution. The insets show the experimental and expected isotopic distribution pattern for $[M – NEt_4]^-$.

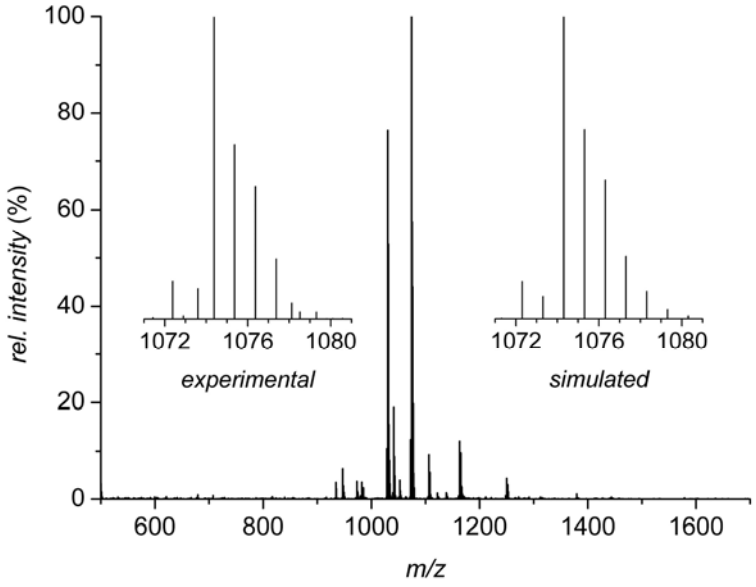

Figure S15: Positive ion ESI-MS spectrum of **4f** in MeCN solution. The insets show the experimental and expected isotopic distribution pattern for $[M + NEt_4]^+$.

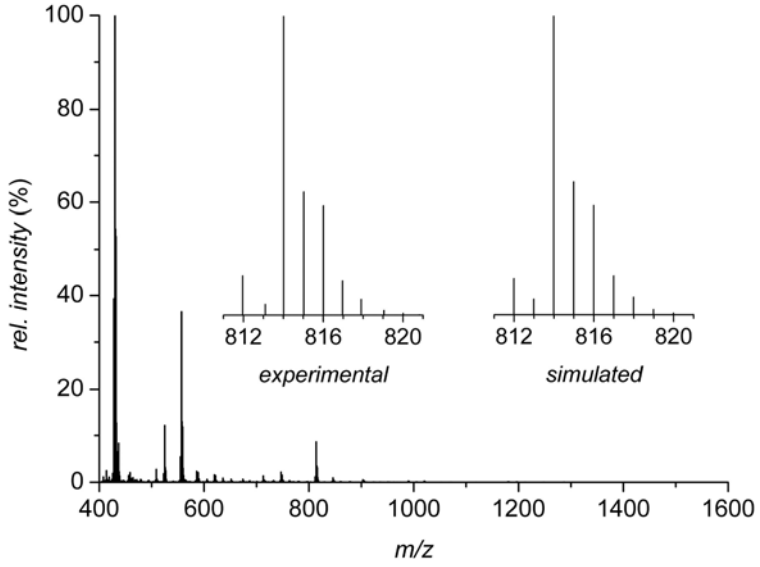

Figure S16: Negative ion ESI-MS spectrum of **4f** in MeCN solution. The insets show the experimental and expected isotopic distribution pattern for $[M – NEt_4]^-$.

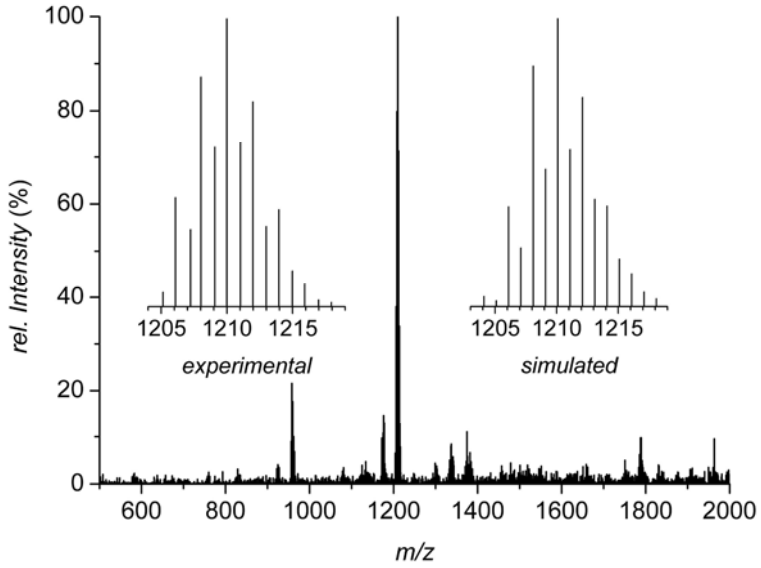

Figure S17: Positive ion ESI-MS spectrum of **5** in MeCN solution. The insets show the experimental and expected isotopic distribution pattern for $[M + NEt_4]^+$.

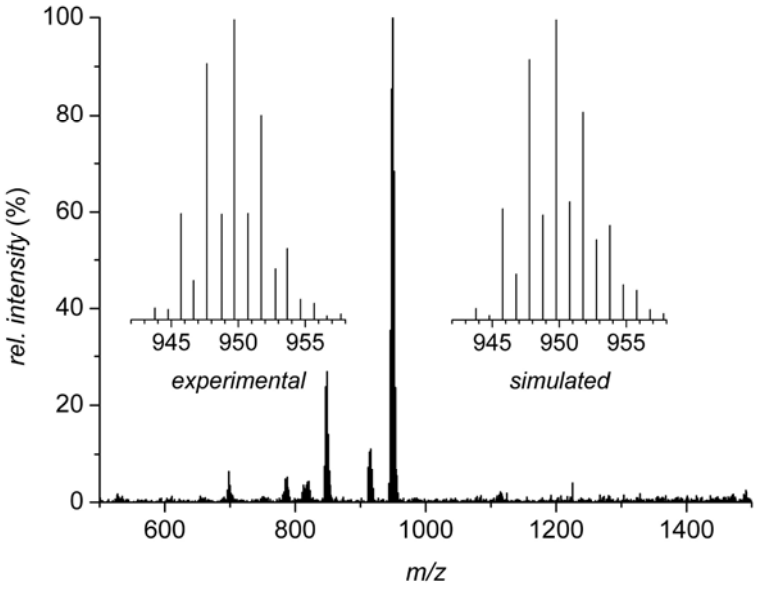

Figure S18: Negative ion ESI-MS spectrum of **5** in MeCN solution. The insets show the experimental and expected isotopic distribution pattern for $[M - NEt_4]^-$.

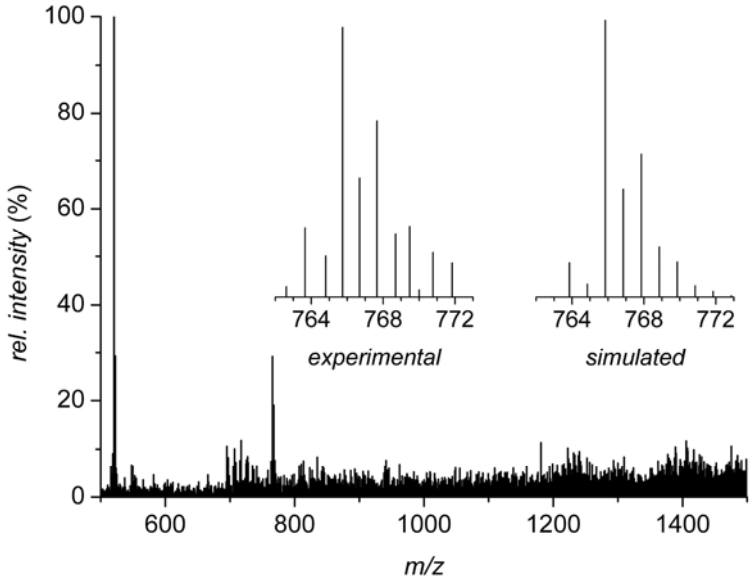

Figure S19: Positive ion ESI-MS spectrum of **6** in MeCN solution. The insets show the experimental and expected isotopic distribution pattern for $[M + NEt_4]^+$.

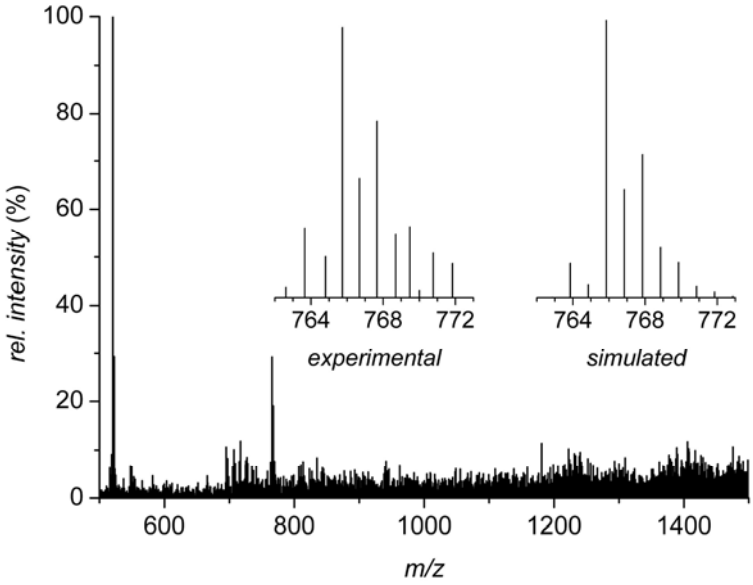

Figure S20: Negative ion ESI-MS spectrum of **6** in MeCN solution. The insets show the experimental and expected isotopic distribution pattern for $[M – NEt_4]^-$.

2. High resolution electrospray ionization mass spectra

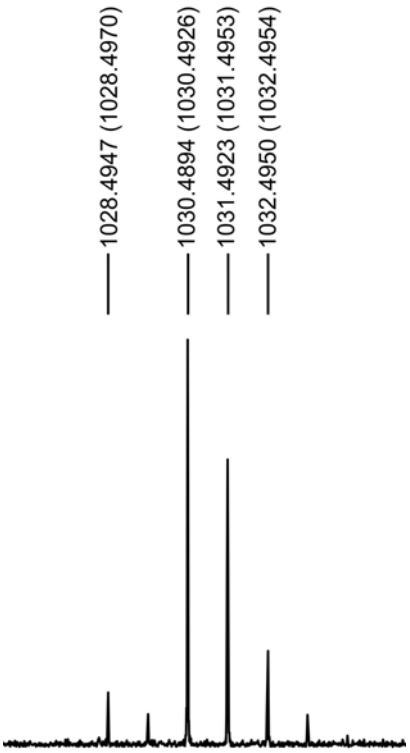

Figure S21: High resolution ESI(+)-MS spectrum of **2** recorded in MeCN at RT. Calculated values for *m/z* are given in parenthesis.

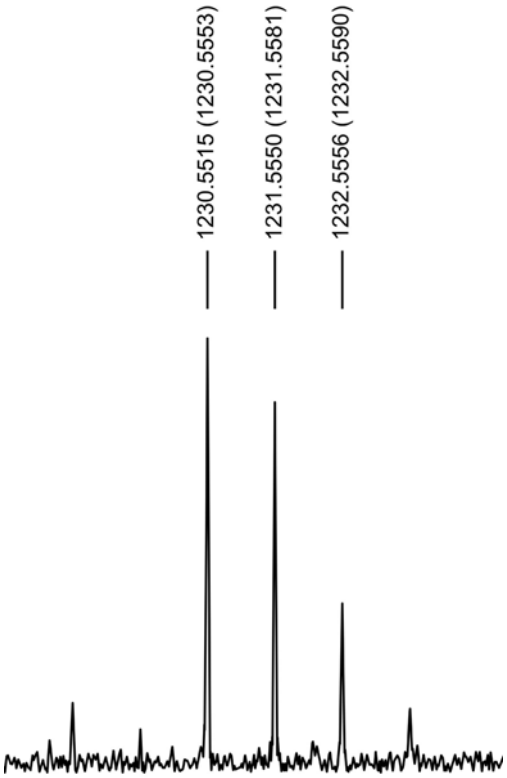

Figure S22: High resolution ESI(+)-MS spectrum of **3** recorded in MeCN at RT. Calculated values for *m/z* are given in parenthesis.

Figure S23: High resolution ESI(+)-MS spectrum of **4a** recorded in MeCN at RT. Calculated values for *m/z* are given in parenthesis.

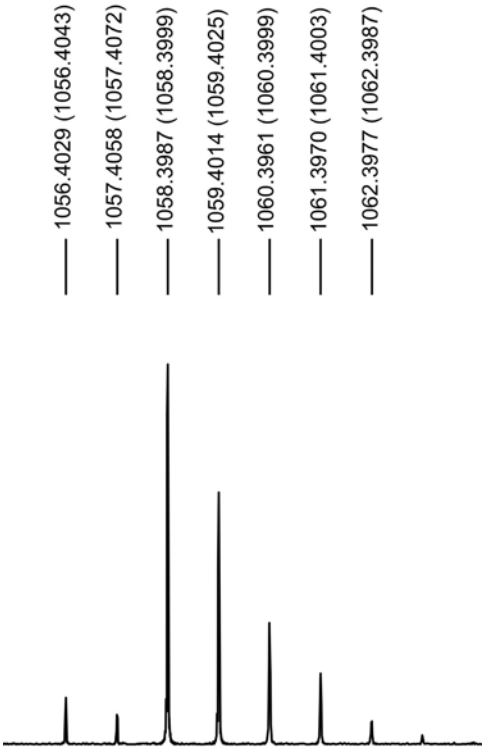

Figure S24: High resolution ESI(+)-MS spectrum of **4b** recorded in MeCN at RT. Calculated values for *m/z* are given in parenthesis.

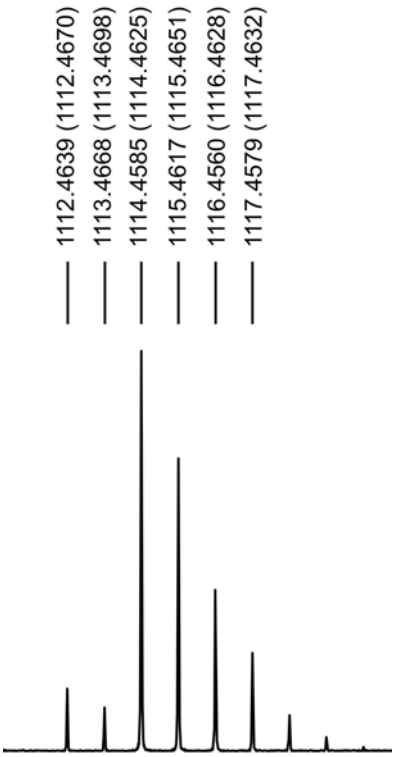

Figure S25: High resolution ESI(+)-MS spectrum of **4c** recorded in MeCN at RT. Calculated values for *m/z* are given in parenthesis.

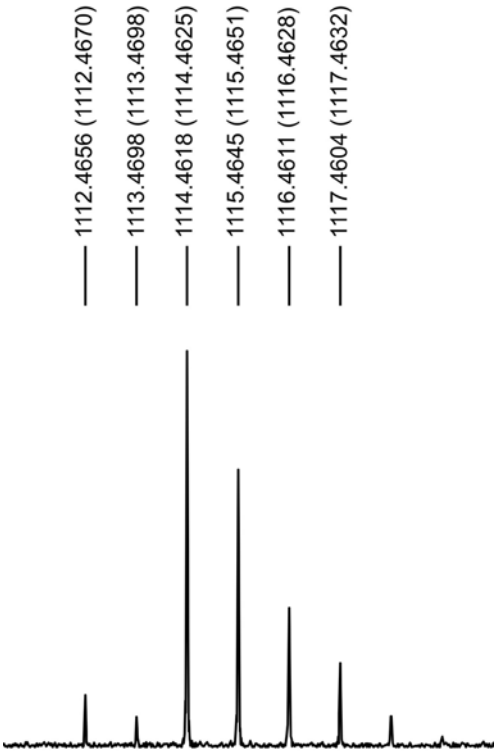

Figure S26: High resolution ESI(+)-MS spectrum of **4d** recorded in MeCN at RT. Calculated values for *m/z* are given in parenthesis.

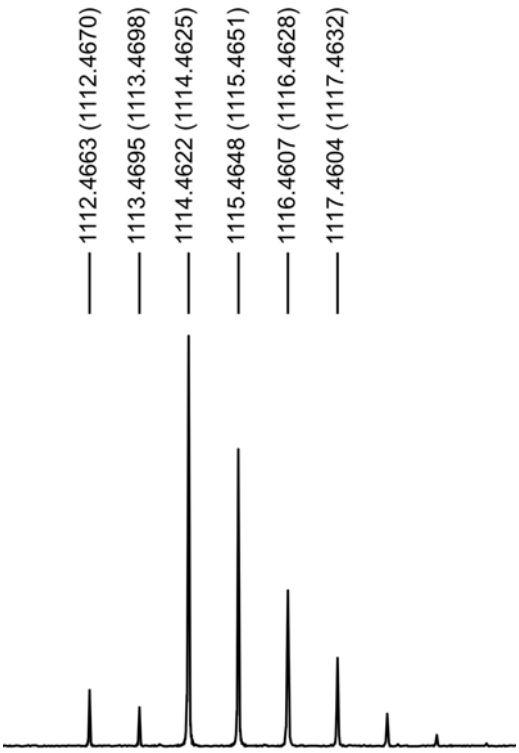

Figure S27: High resolution ESI(+)-MS spectrum of **4e** recorded in MeCN at RT. Calculated values for *m/z* are given in parenthesis.

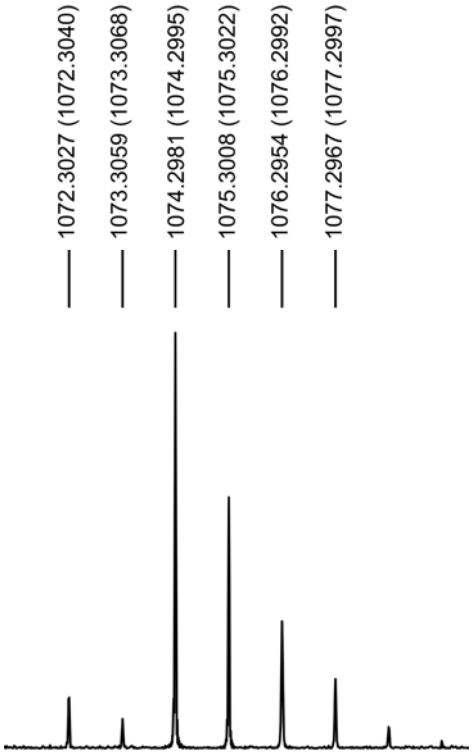

Figure S28: High resolution ESI(+)-MS spectrum of **4f** recorded in MeCN at RT. Calculated values for *m/z* are given in parenthesis.

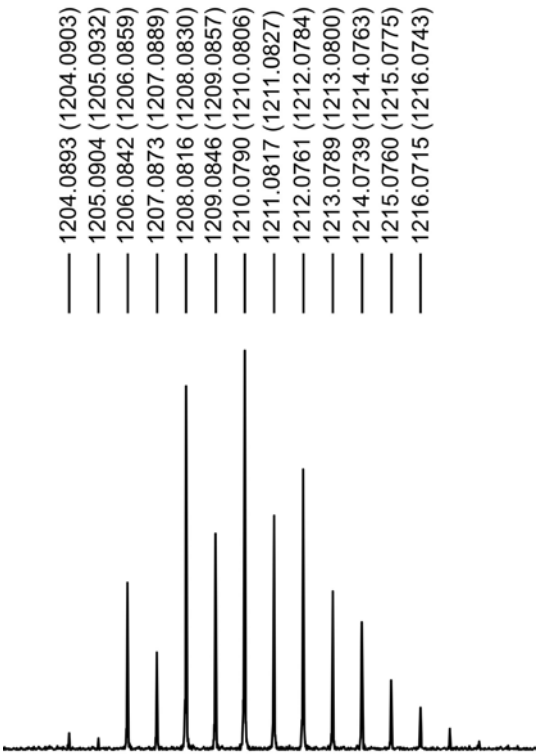

Figure S29: High resolution ESI(+)-MS spectrum of **5** recorded in MeCN at RT. Calculated values for *m/z* are given in parenthesis.

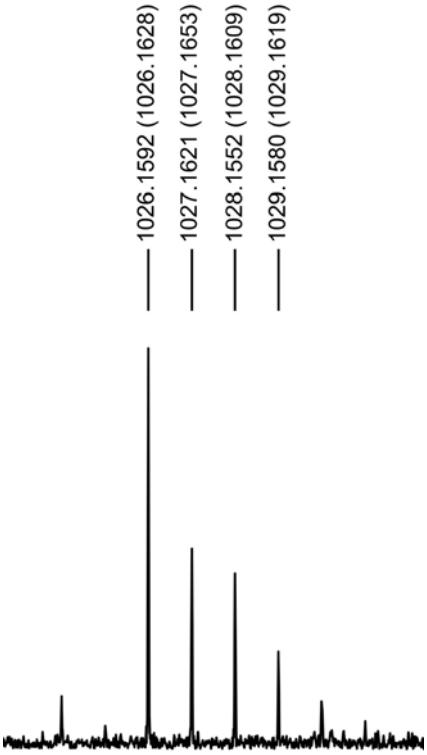

Figure S30: High resolution ESI(+)-MS spectrum of **6** recorded in MeCN at RT. Calculated values for *m/z* are given in parenthesis.

3. NMR spectra

Typically, an acquisition of proton NMR spectra for synthetic [2Fe-2S] clusters is feasible, due to the strong antiferromagnetic coupling between both ferric ions (ferromagnetically coupled [2Fe-2S] clusters have not been synthesized, yet). However, magnetic moments at room temperature cause a broadening of all signals to an extend that fine-structures (*i.e.* H,H-couplings) are usually unresolved. Peak shapes and integrals depend on the protons' distances from the paramagnetic cluster core. Therefore integrals are relatively vague. Resonances from protons in close proximity to the metal centres are often extremely broadened and fade away in the baseline noise.

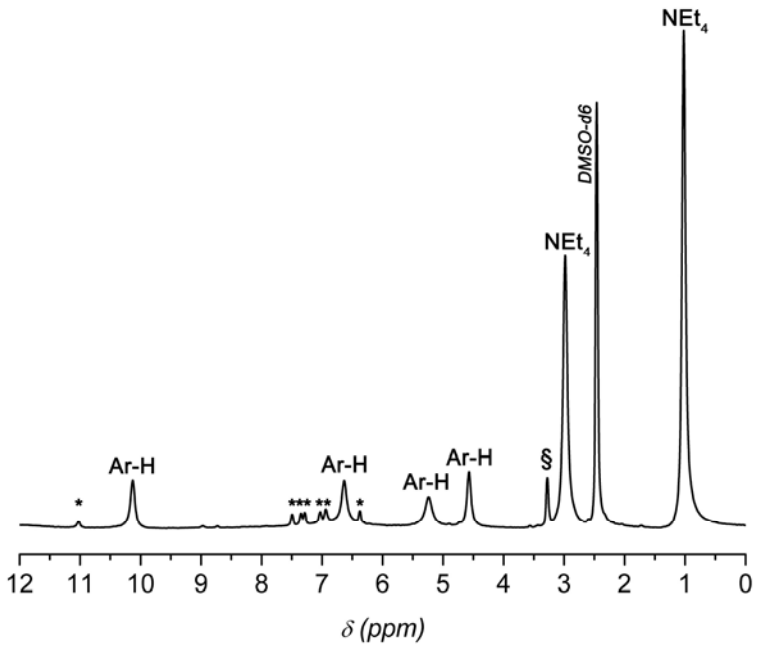

Figure S31: Proton NMR spectrum (500MHz, RT) of **2** in DMSO-d_6. Signals corresponding to free indole (marked by *) and an unidentified impurity (marked by §) appear upon dissolution of **2** in DMSO-d_6, due to the lability of the cluster in this solvent.

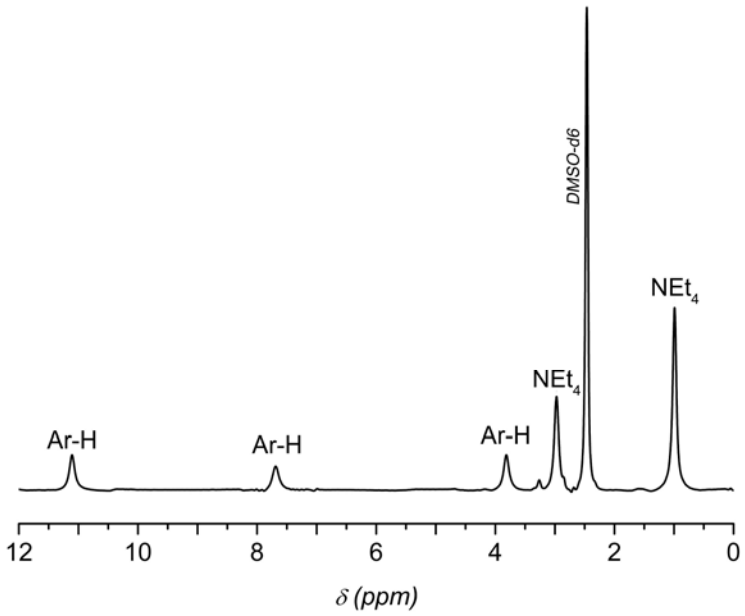

Figure S32: Proton NMR spectrum (500MHz, RT) of **3** in DMSO-d_6.

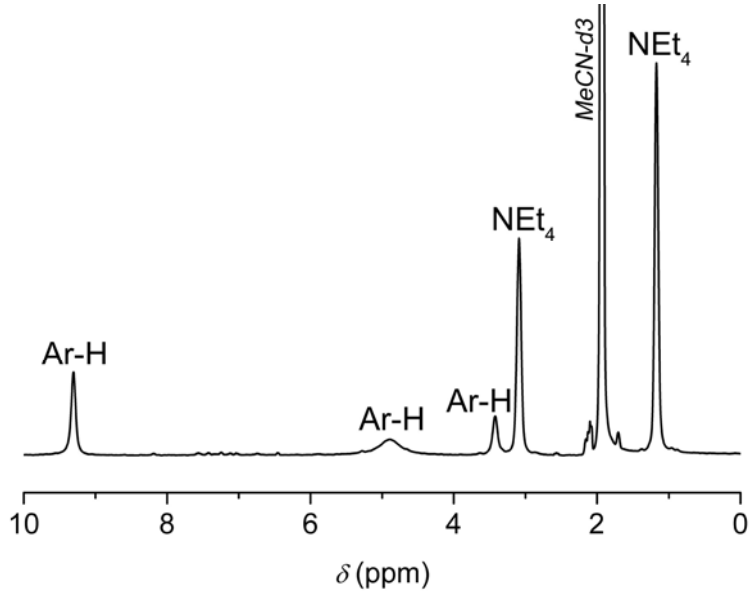

Figure S33: Proton NMR spectrum (300MHz, RT) of **4a** in MeCN-d_3.

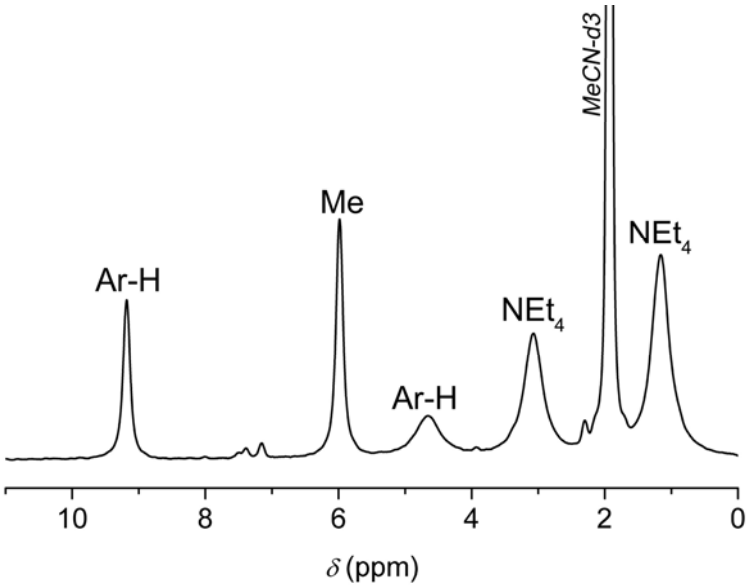

Figure S34: Proton NMR spectrum (300MHz, RT) of **4b** in MeCN-d_3.

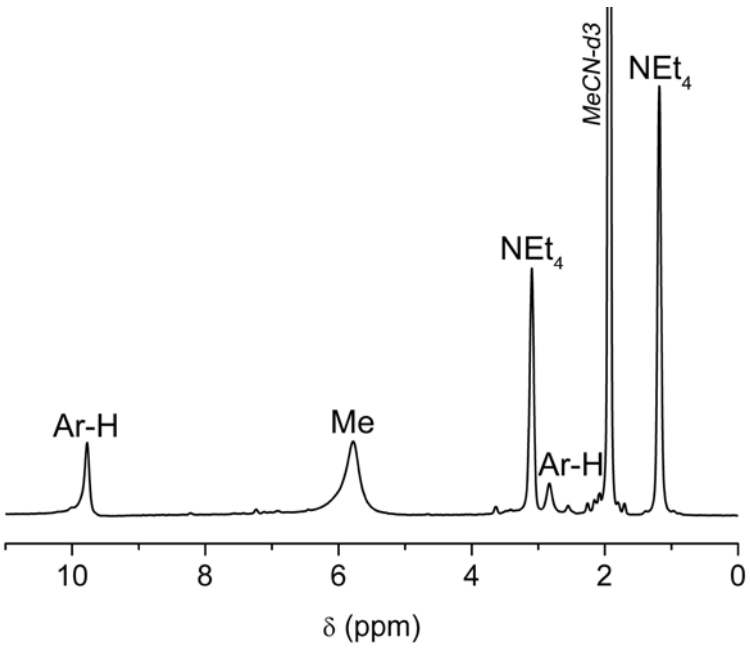

Figure S35: Proton NMR spectrum (300MHz, RT) of **4c** in MeCN-d_3.

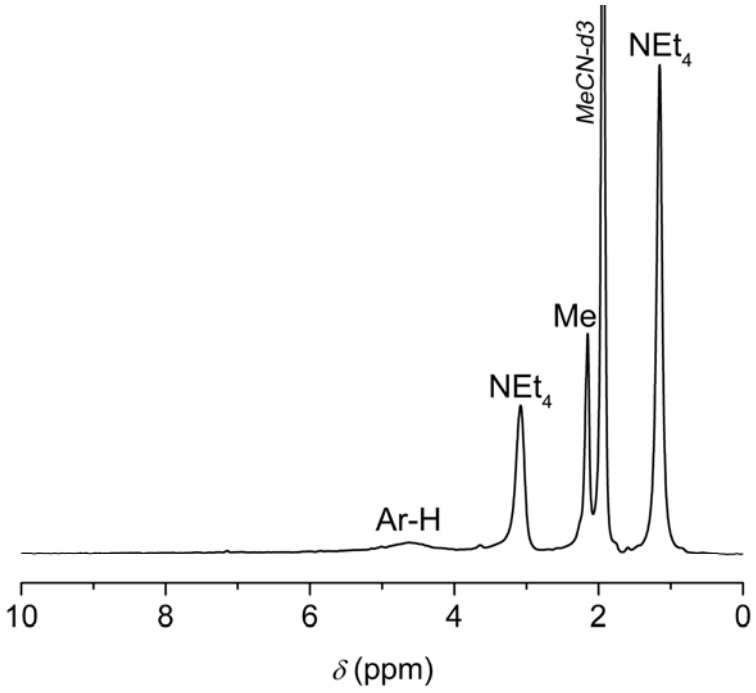

Figure S36: Proton NMR spectrum (300MHz, RT) of **4d** in MeCN-d_3.

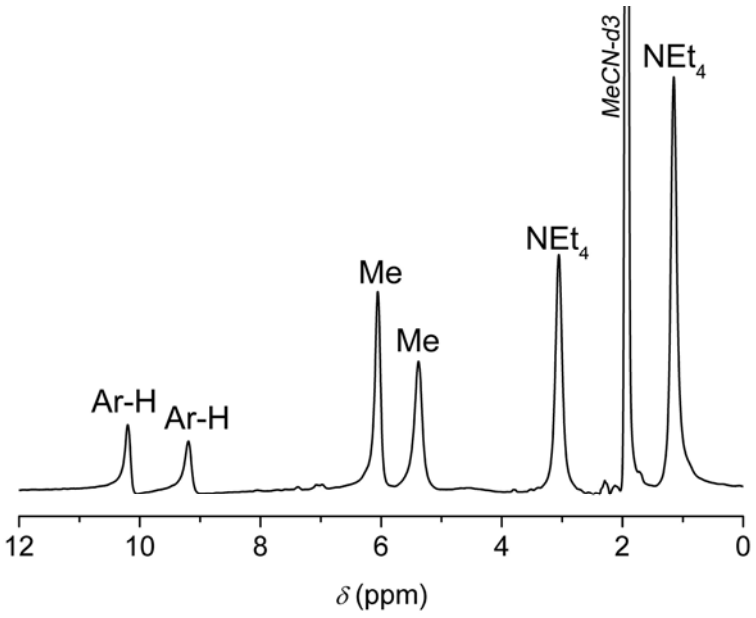

Figure S37: Proton NMR spectrum (300MHz, RT) of **4e** in MeCN-d_3.

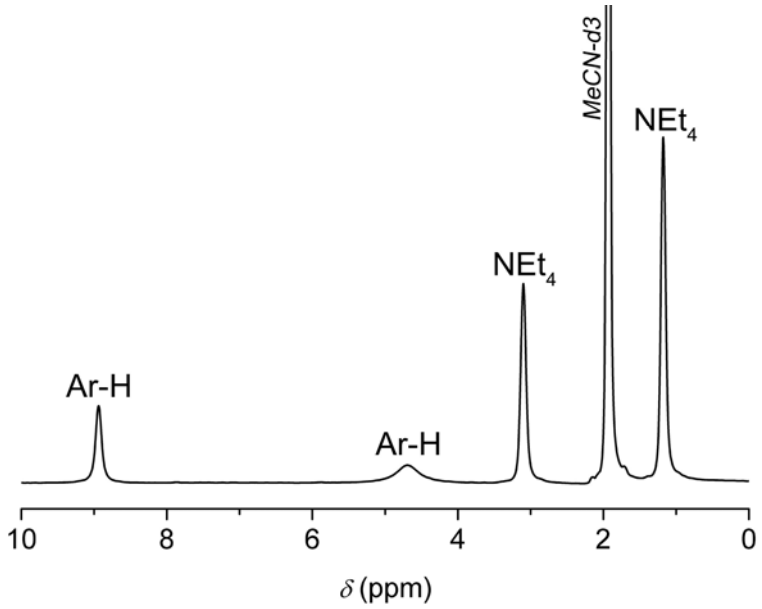

Figure S38: Proton NMR spectrum (300MHz, RT) of **4f** in MeCN-d_3.

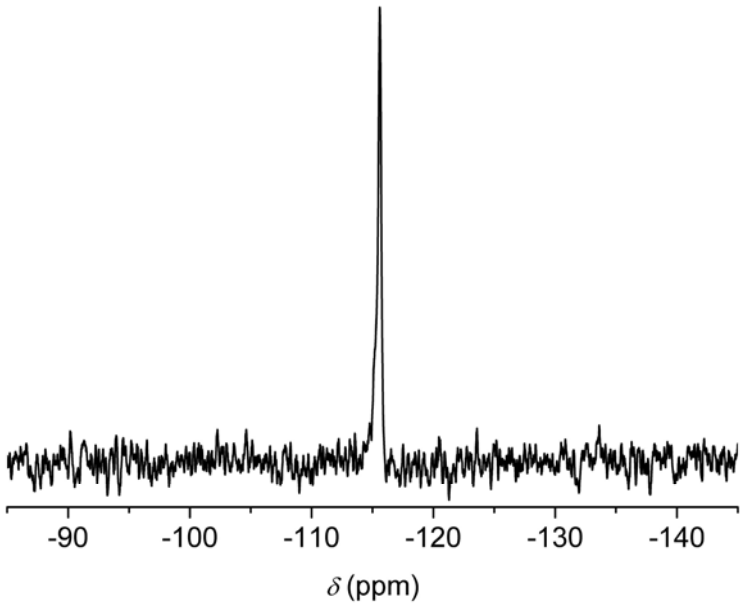

Figure S39: ^{19}F NMR spectrum (188MHz, RT) of **4f** in MeCN-d_3 (referenced to $CFCl_3$).

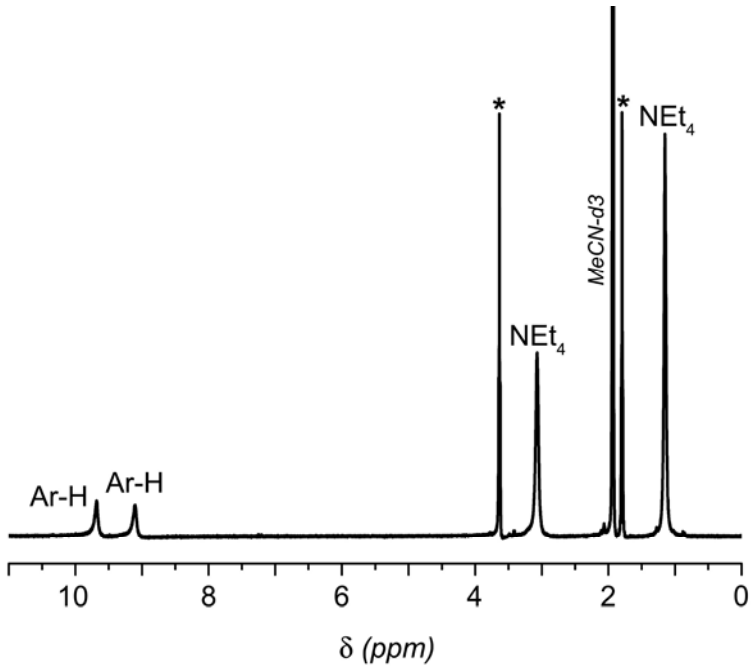

Figure S40: Proton NMR spectrum (500MHz, RT) of **5** in MeCN-d_3. Residual THF signals are marked by *.

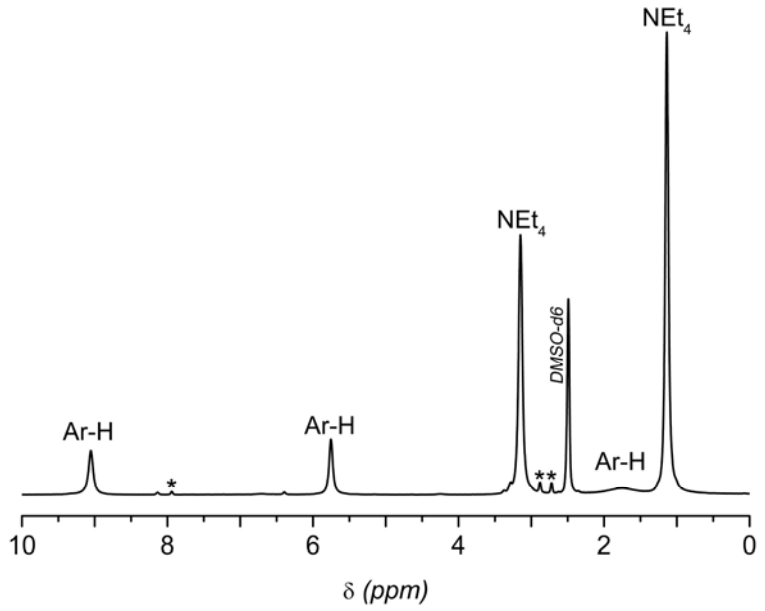

Figure S41: Proton NMR spectrum (500MHz, RT) of **6** in DMSO-d_6. Residual DMF signals are marked by *.

4. Electrochemical measurements

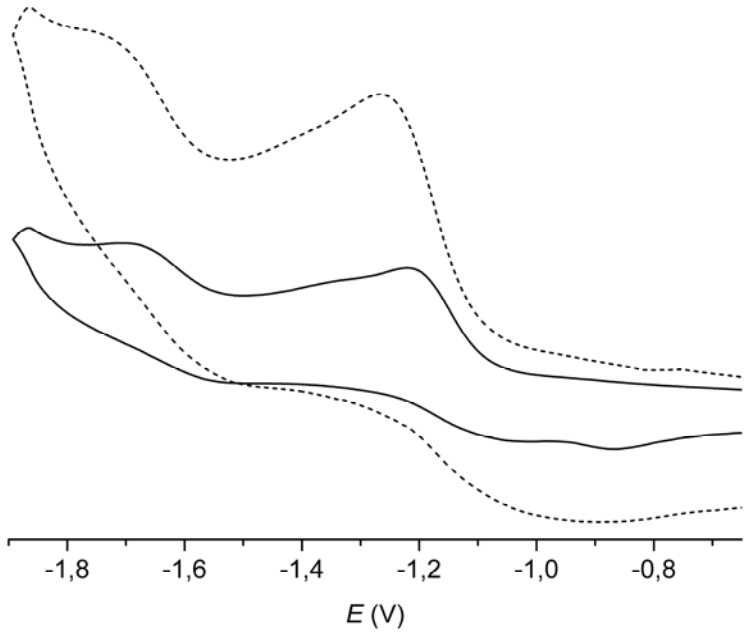

Figure S42: Cyclic voltamogram of **2** in DMF/0.1 M NBu_4PF_6 solution at scan rates of 100 mVs^{-1} (solid line) and 500 mVs^{-1} (dashed line). Potentials are given in volts *vs.* the $Cp^*_2Fe/Cp^*_2Fe^+$ couple.

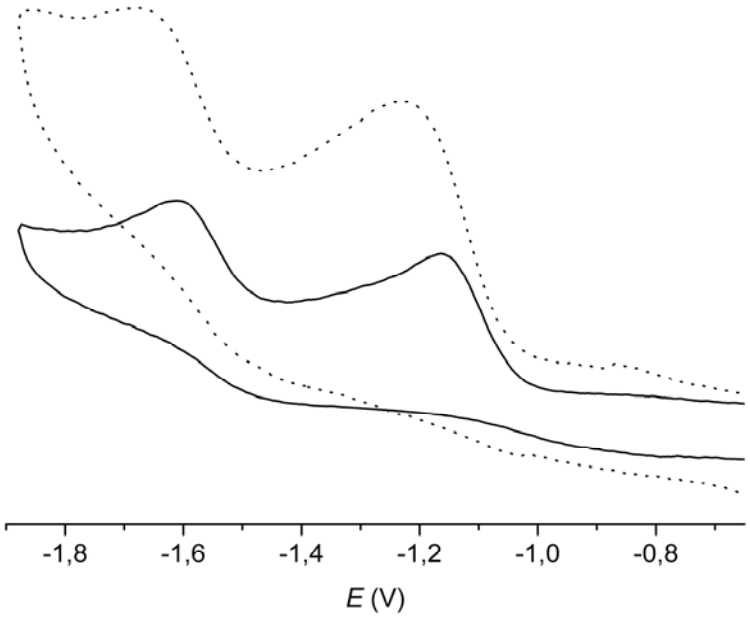

Figure S43: Cyclic voltamogram of **3** in DMF/0.1 M NBu_4PF_6 solution at scan rates of 100 mVs^{-1} (solid line) and 500 mVs^{-1} (dashed line). Potentials are given in volts *vs.* the $Cp^*_2Fe/Cp^*_2Fe^+$ couple.

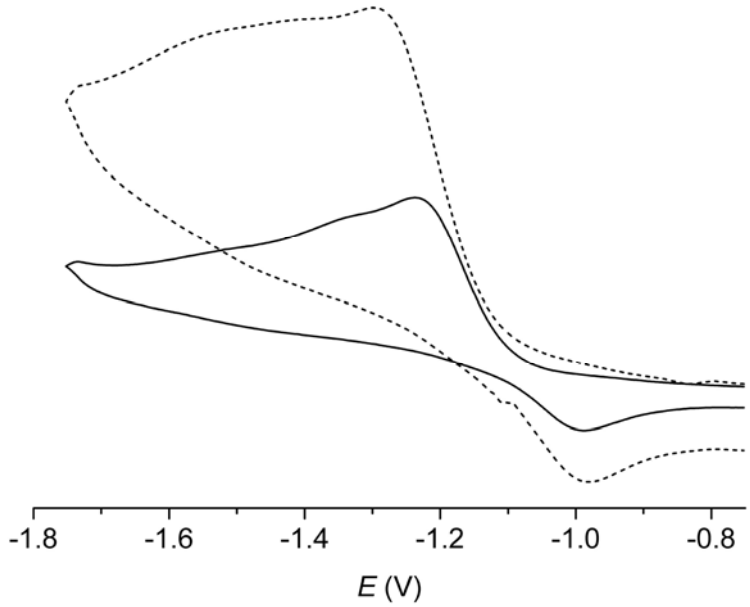

Figure S44: Cyclic voltamogram of **4a** in MeCN/0.1 M NBu_4PF_6 solution at scan rates of 100 mVs^{-1} (solid line) and 500 mVs^{-1} (dashed line). Potentials are given in volts *vs.* the $Cp^*_2Fe/Cp^*_2Fe^+$ couple.

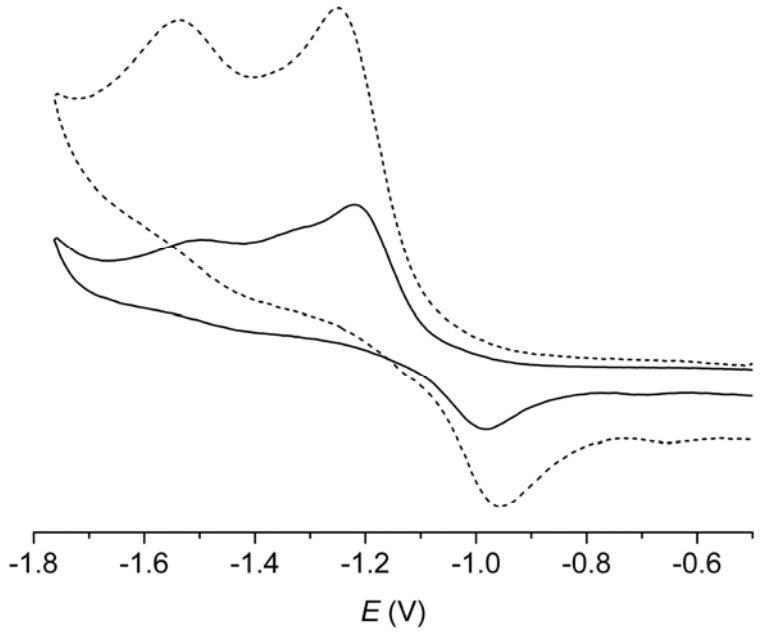

Figure S45: Cyclic voltamogram of **4b** in MeCN/0.1 M NBu_4PF_6 solution at scan rates of 100 mVs^{-1} (solid line) and 500 mVs^{-1} (dashed line). Potentials are given in volts *vs.* the $Cp^*_2Fe/Cp^*_2Fe^+$ couple.

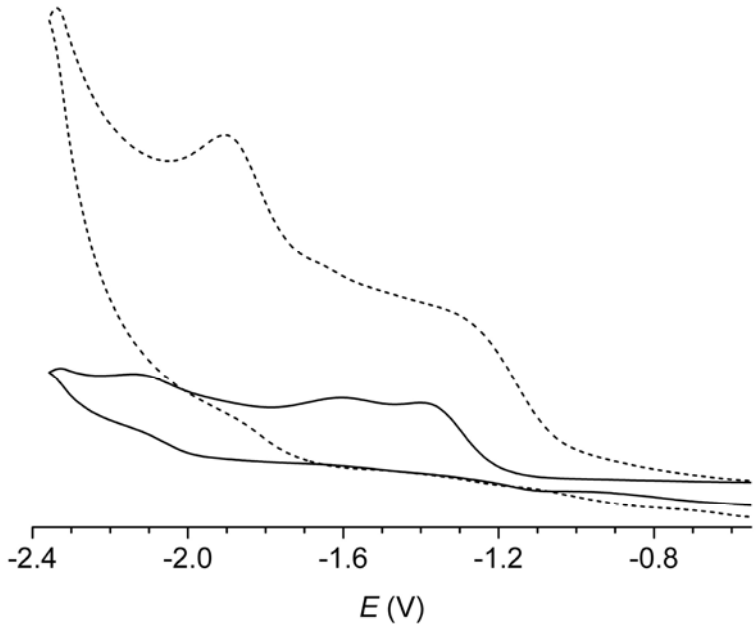

Figure S46: Cyclic voltamogram of **4c** in MeCN/0.1 M NBu_4PF_6 solution at scan rates of 100 mVs^{-1} (solid line) and 500 mVs^{-1} (dashed line). Potentials are given in volts *vs.* the $Cp^*_2Fe/Cp^*_2Fe^+$ couple.

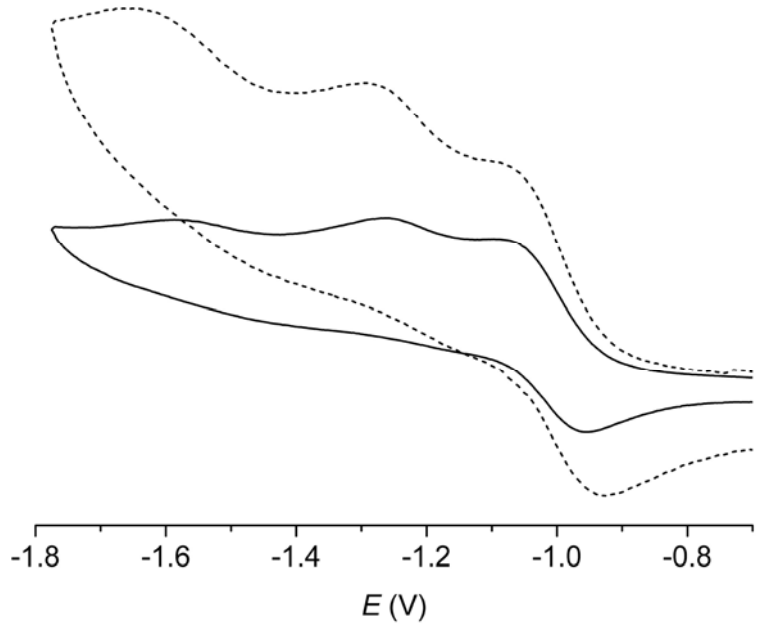

Figure S47: Cyclic voltamogram of **4d** in MeCN/0.1 M NBu_4PF_6 solution at scan rates of 100 mVs^{-1} (solid line) and 500 mVs^{-1} (dashed line). Potentials are given in volts *vs.* the $Cp^*_2Fe/Cp^*_2Fe^+$ couple.

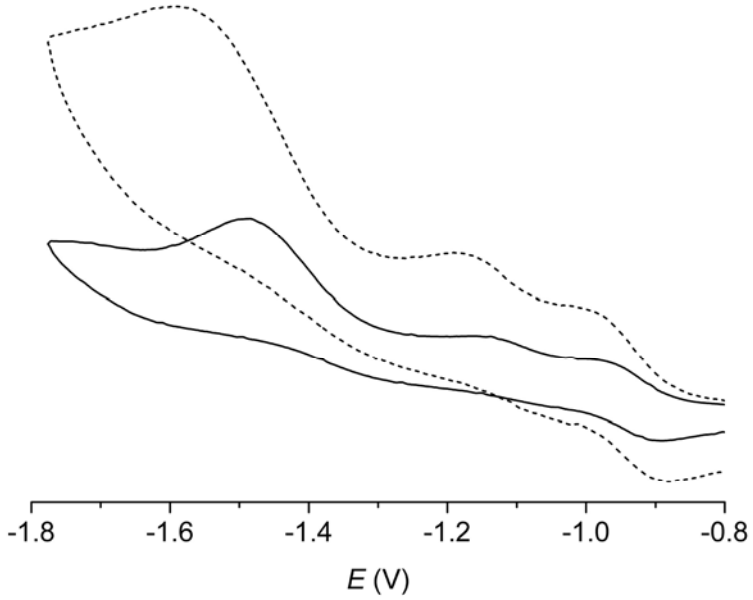

Figure S48: Cyclic voltamogram of **4e** in MeCN/0.1 M NBu_4PF_6 solution at scan rates of 100 mVs^{-1} (solid line) and 500 mVs^{-1} (dashed line). Potentials are given in volts *vs.* the $Cp^*_2Fe/Cp^*_2Fe^+$ couple.

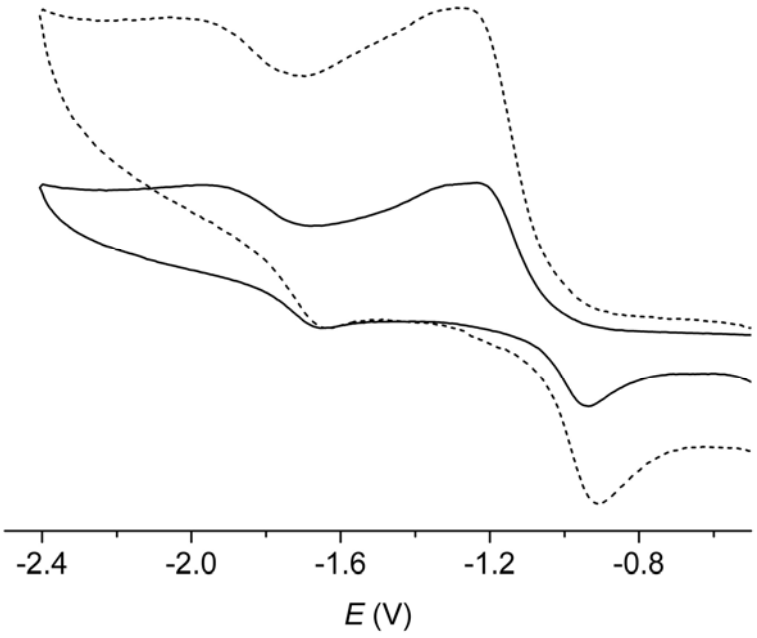

Figure S49: Cyclic voltamogram of **4f** in MeCN/0.1 M NBu_4PF_6 solution at scan rates of 100 mVs^{-1} (solid line) and 500 mVs^{-1} (dashed line). Potentials are given in volts *vs.* the $Cp^*_2Fe/Cp^*_2Fe^+$ couple.

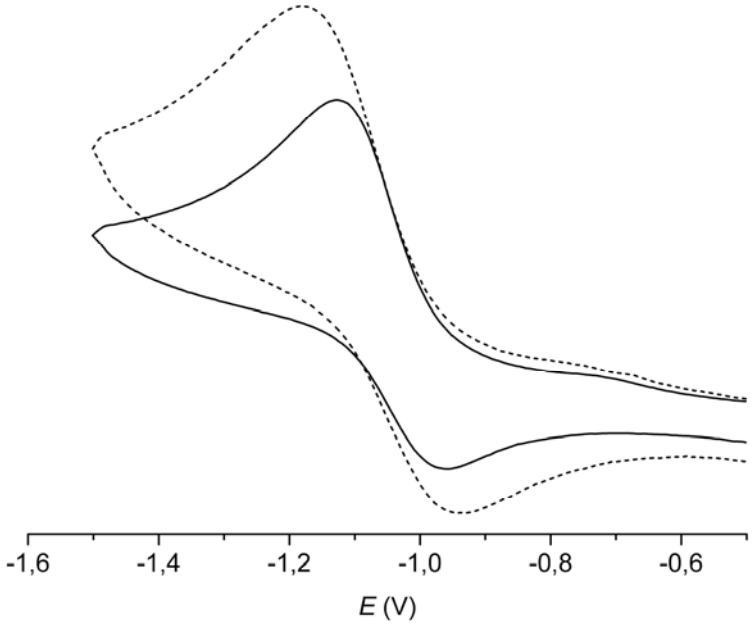

Figure S50: Cyclic voltamogram of **5** in MeCN/0.1 M NBu_4PF_6 solution at scan rates of 100 mVs^{-1} (solid line) and 500 mVs^{-1} (dashed line). Potentials are given in volts *vs.* the $Cp^*_2Fe/Cp^*_2Fe^+$ couple.

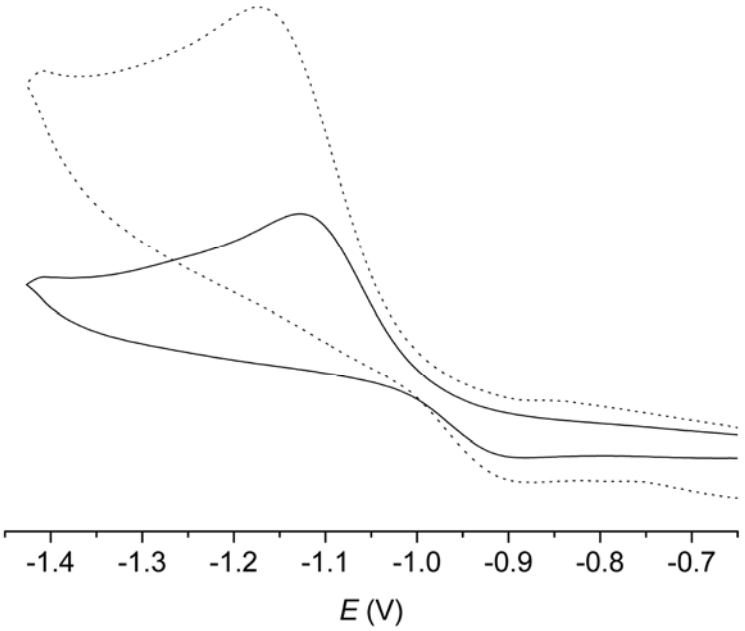

Figure S51: Cyclic voltamogram of **6** in DMF/0.1 M NBu_4PF_6 solution at scan rates of 100 mVs^{-1} (solid line) and 500 mVs^{-1} (dashed line). Potentials are given in volts *vs.* the $Cp^*_2Fe/Cp^*_2Fe^+$ couple.

5. UV-Vis spectra

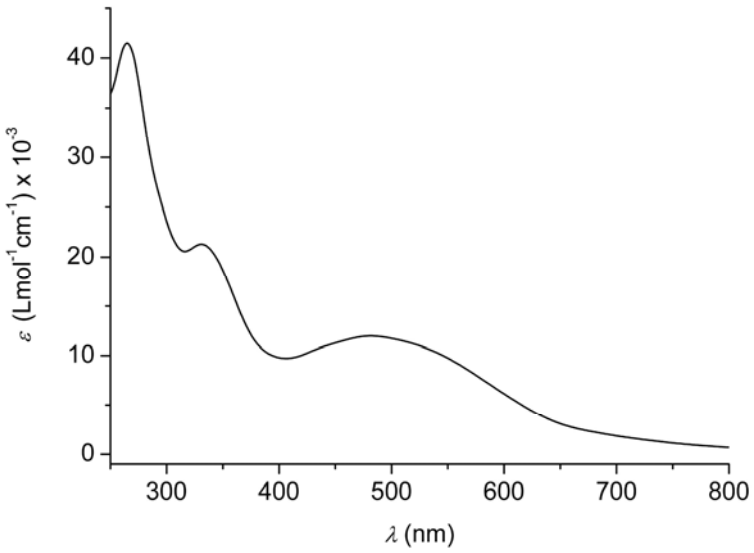

Figure S52: Electronic absorption spectrum of **4a** recorded in MeCN solution at room temperature.

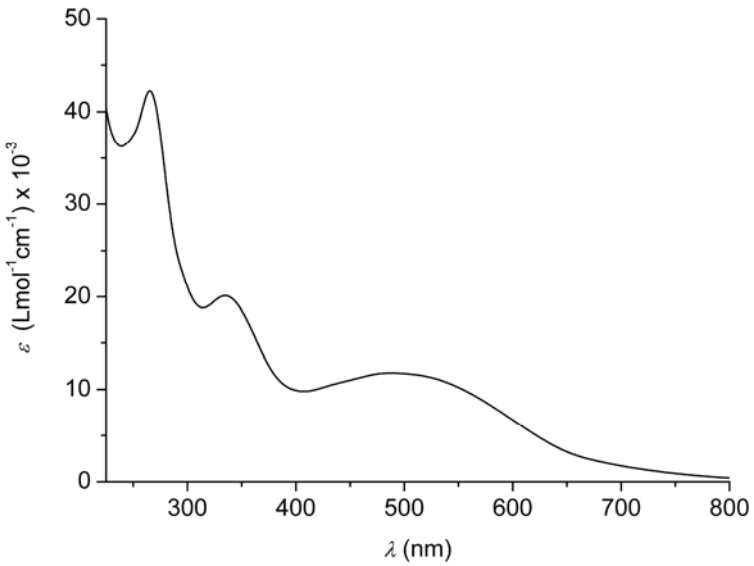

Figure S53: Electronic absorption spectrum of **4b** recorded in MeCN solution at room temperature.

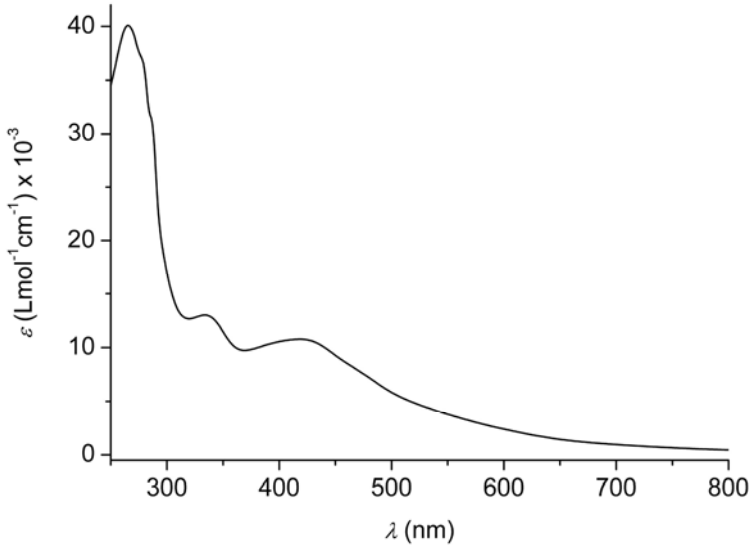

Figure S54: Electronic absorption spectrum of **4c** recorded in MeCN solution at room temperature.

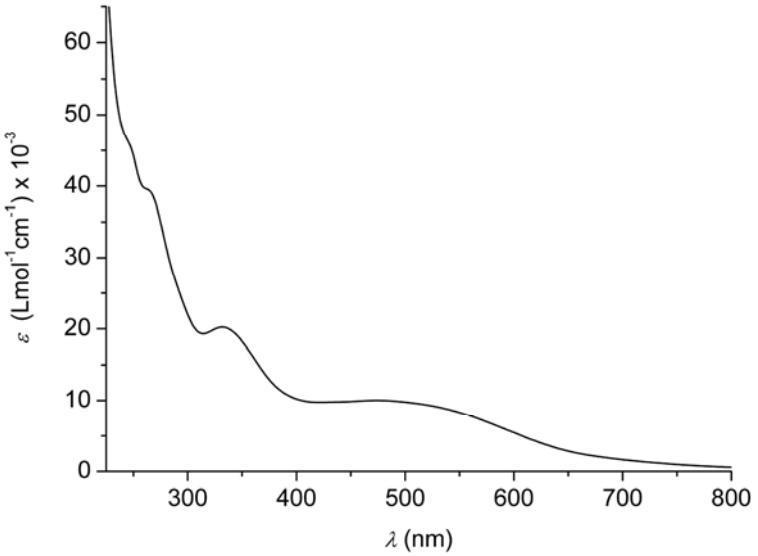

Figure S55: Electronic absorption spectrum of **4d** recorded in MeCN solution at room temperature.

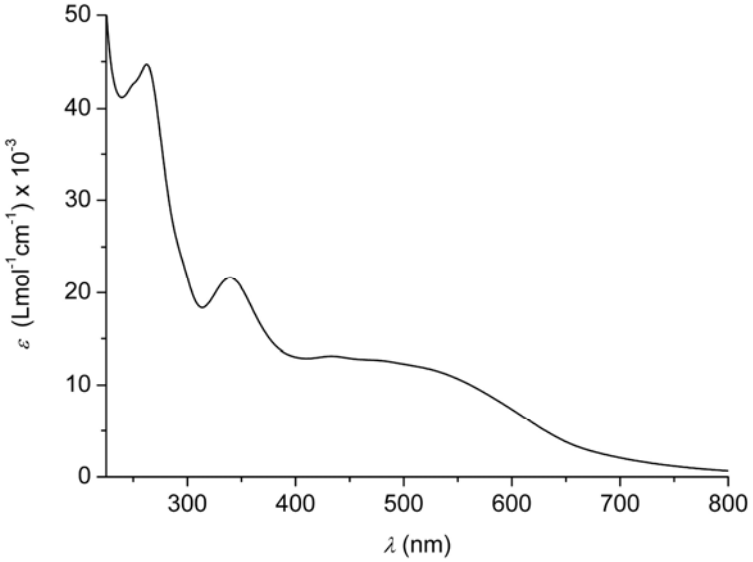

Figure S56: Electronic absorption spectrum of **4e** recorded in MeCN solution at room temperature.

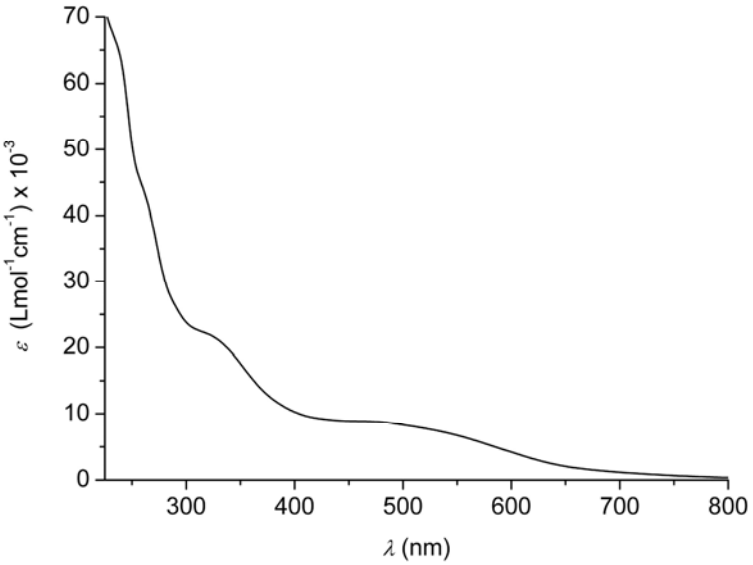

Figure S57: Electronic absorption spectrum of **4f** recorded in MeCN solution at room temperature.

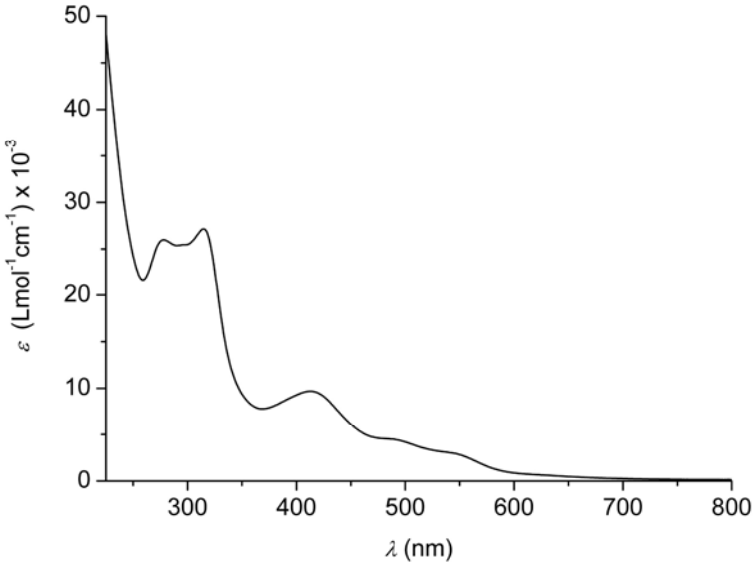

Figure S58: Electronic absorption spectrum of **5** recorded in MeCN solution at room temperature.

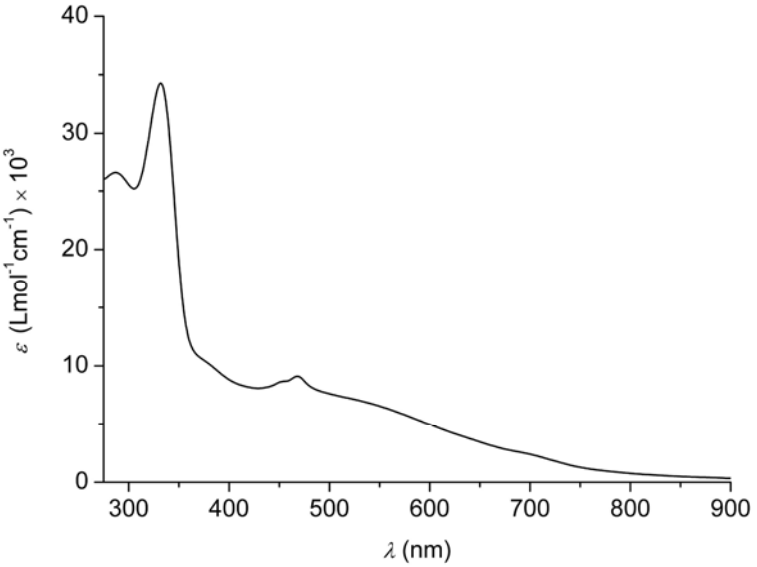

Figure S59: Electronic absorption spectrum of **6** recorded in DMF solution at room temperature.

6. Magnetic susceptibility measurements (SQUID)

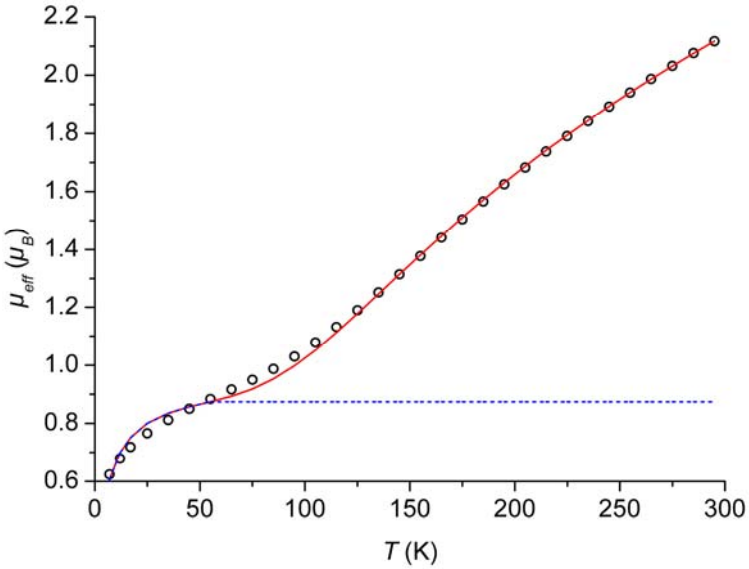

Figure S60: Plot of μ_{eff} (μ_B) *vs.* temperature for **2** at a magnetic field B = 0.5 T. The red solid line is fitted to the experimental values (circles), taking a paramagnetic impurity *PI* (monomeric iron (III), S = 5/2) into account (blue dotted line). Best fit parameters: J = –159 cm^{-1}, *PI* = 2.6%, χ(*TIP*) = 7.3 ·10^{-6} cm^{3}mol^{-1} (subtracted), g = 2.000 (fixed), θ_{mono} = –10.0 K (fixed).

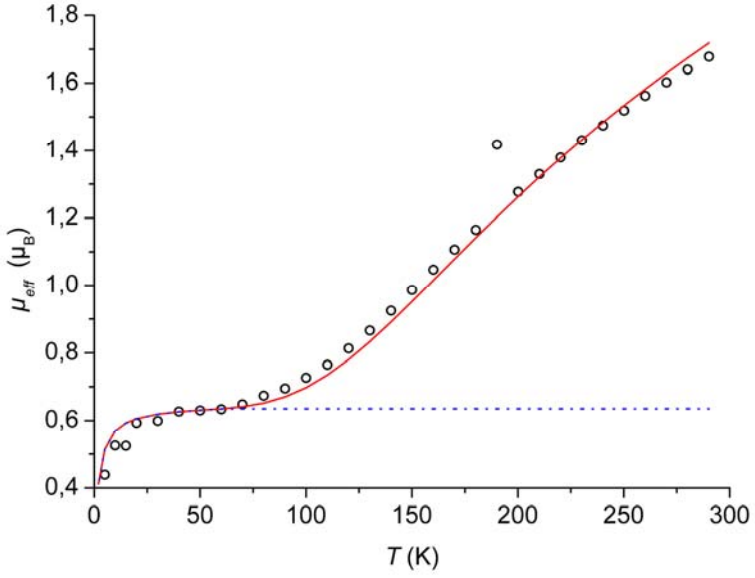

Figure S61: Plot of μ_{eff} (μ_B) *vs.* temperature for **3** at a magnetic field B = 1 T. The red solid line is fitted to the experimental values (circles), taking a paramagnetic impurity *PI* (monomeric iron (III), S = 5/2) into account (blue dotted line). Best fit parameters: J = –199 cm^{-1}, *PI* = 1.2%, χ(*TIP*) = 760 ·10^{-6} cm^{3}mol^{-1} (subtracted), g = 2.000 (fixed), θ_{mono} = –3.0 K (fixed).

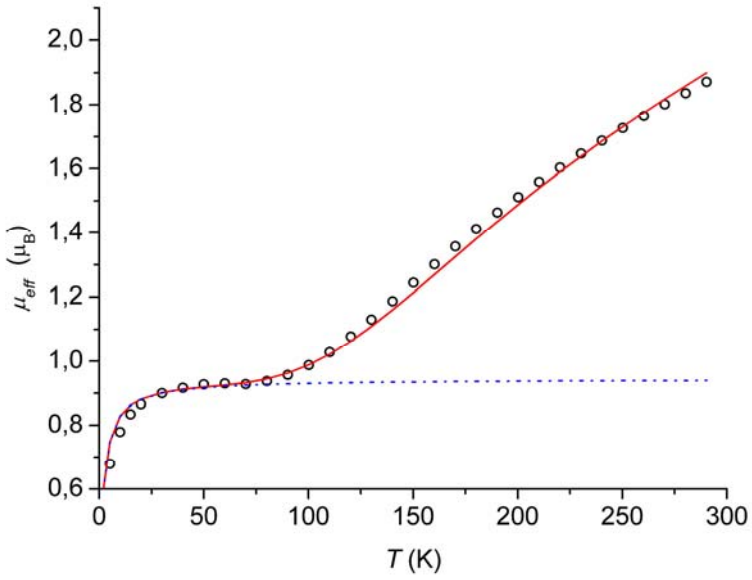

Figure S62: Plot of μ_{eff} (μ_B) *vs.* temperature for **5** at a magnetic field B = 1 T. The red solid line is fitted to the experimental values (circles), taking a paramagnetic impurity *PI* (monomeric iron (III), S = 5/2) into account (blue dotted line). Best fit parameters: J = –188 cm^{-1}, *PI* = 2.5%, χ(*TIP*) = 350 ·10^{-6} cm^{3}mol^{-1} (subtracted), g = 2.000 (fixed), θ_{mono} = –3.0 K (fixed).

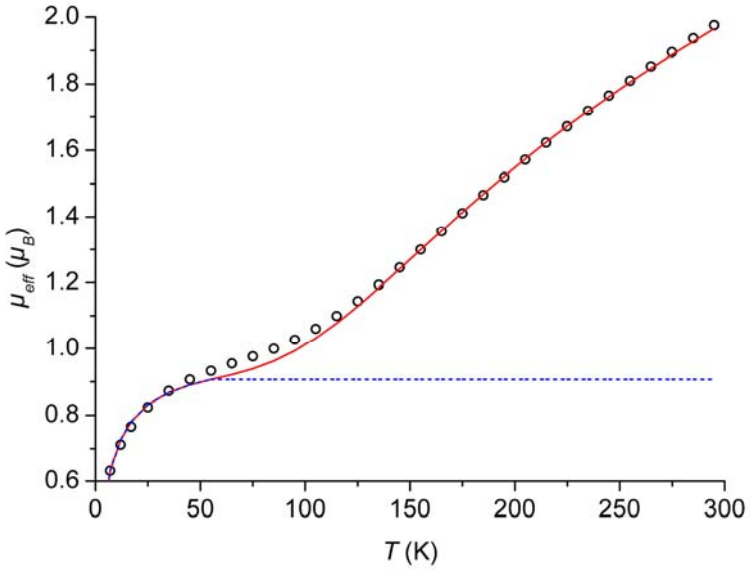

Figure S63: Plot of μ_{eff} (μ_B) *vs.* temperature for **6** at a magnetic field B = 0.5 T. The red solid line is fitted to the experimental values (circles), taking a paramagnetic impurity *PI* (monomeric iron (III), S = 5/2) into account (blue dotted line). Best fit parameters: J = –176 cm^{-1}, *PI* = 2.8%, χ(*TIP*) = 104.1 ·10^{-6} cm^{3}mol^{-1} (subtracted), g = 2.000 (fixed), θ_{mono} = –10.0 K (fixed).

7. Zero-field Mössbauer spectra

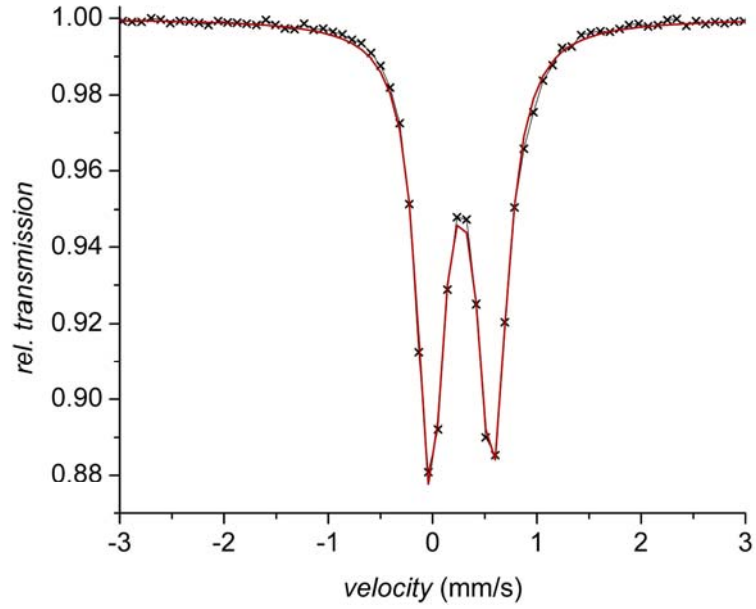

Figure S64: Zero-field Mössbauer spectrum of **2** at 80 K, referenced to ^{57}Fe metal at room temperature. The solid lines are Lorentzian doublets fitted to the experimental values (crosses).

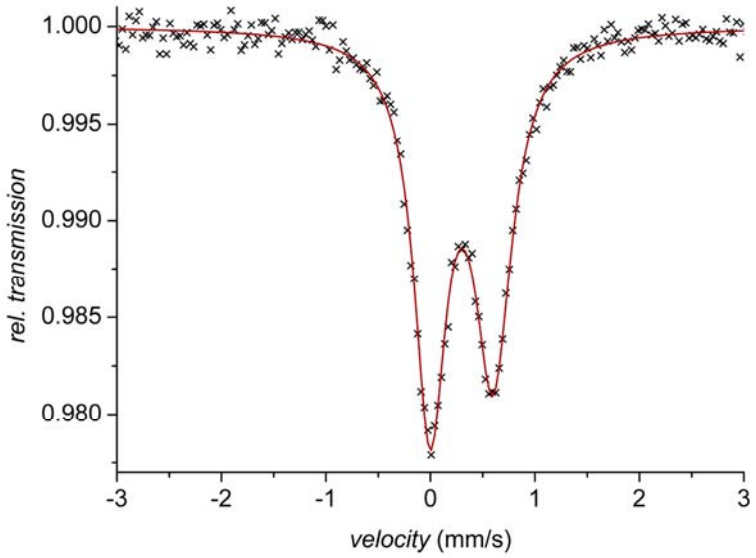

Figure S65: Zero-field Mössbauer spectrum of **3** at 80 K, referenced to ^{57}Fe metal at room temperature. The solid lines are Lorentzian doublets fitted to the experimental values (crosses).

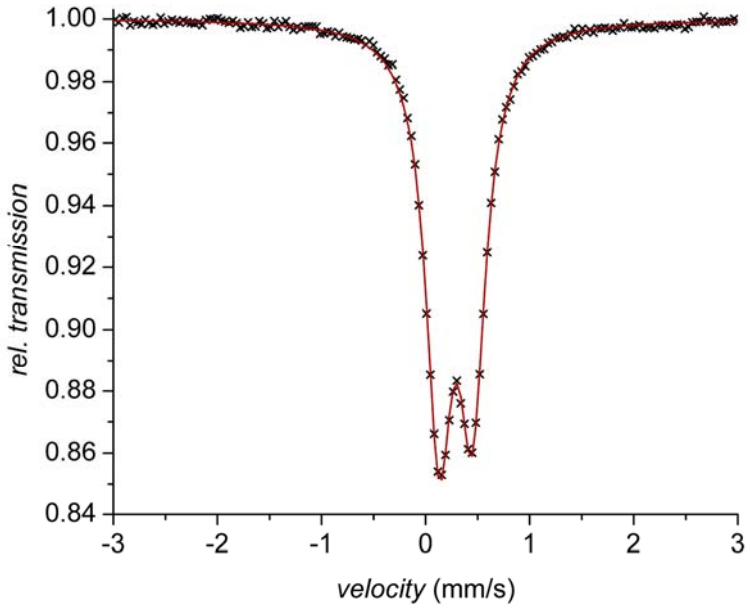

Figure S66: Zero-field Mössbauer spectrum of **4a** at 80 K, referenced to ^{57}Fe metal at room temperature. The solid lines are Lorentzian doublets fitted to the experimental values (crosses).

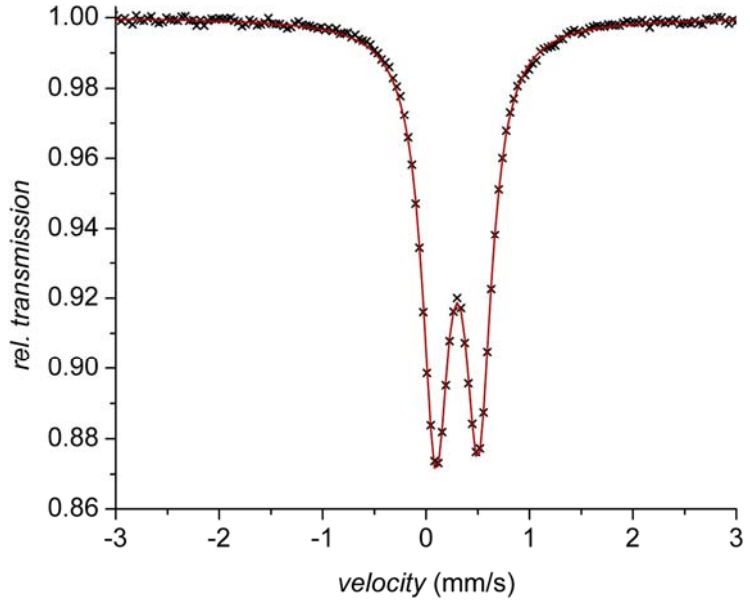

Figure S67: Zero-field Mössbauer spectrum of **4b** at 80 K, referenced to ^{57}Fe metal at room temperature. The solid lines are Lorentzian doublets fitted to the experimental values (crosses).

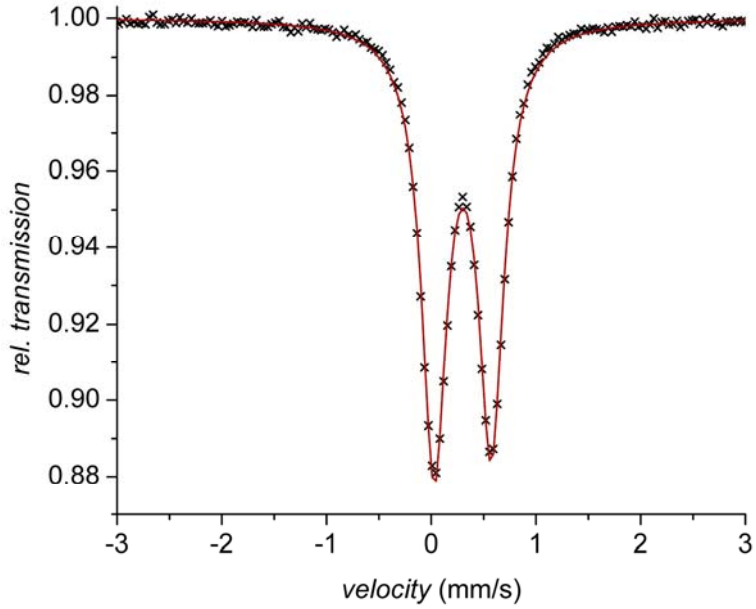

Figure S68: Zero-field Mössbauer spectrum of **4c** at 80 K, referenced to ^{57}Fe metal at room temperature. The solid lines are Lorentzian doublets fitted to the experimental values (crosses).

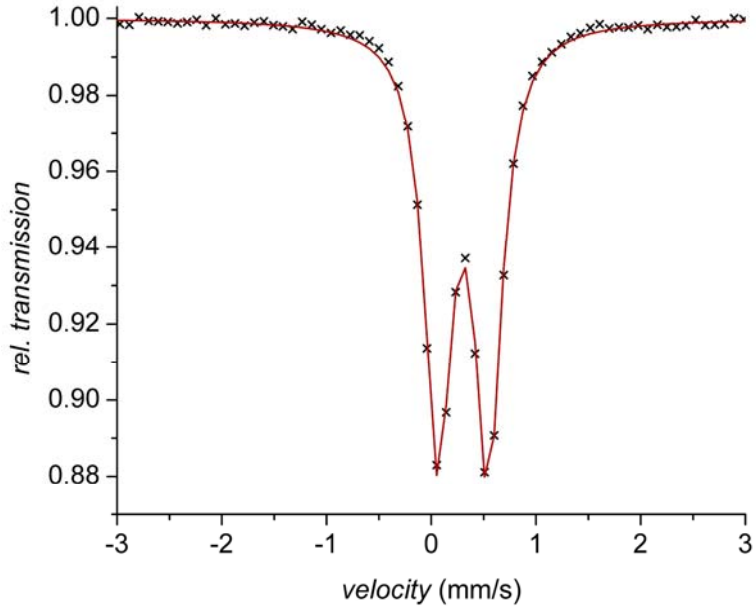

Figure S69: Zero-field Mössbauer spectrum of **4d** at 80 K, referenced to ^{57}Fe metal at room temperature. The solid lines are Lorentzian doublets fitted to the experimental values (crosses).

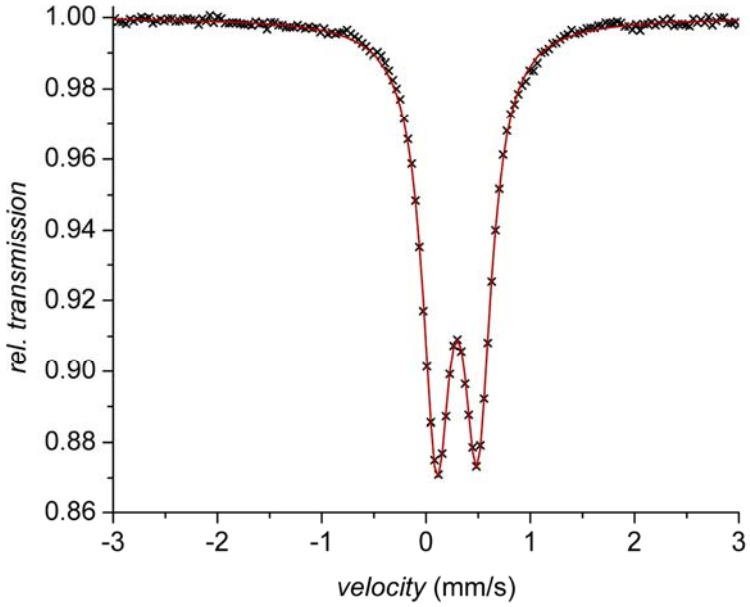

Figure S70: Zero-field Mössbauer spectrum of **4e** at 80 K, referenced to ^{57}Fe metal at room temperature. The solid lines are Lorentzian doublets fitted to the experimental values (crosses).

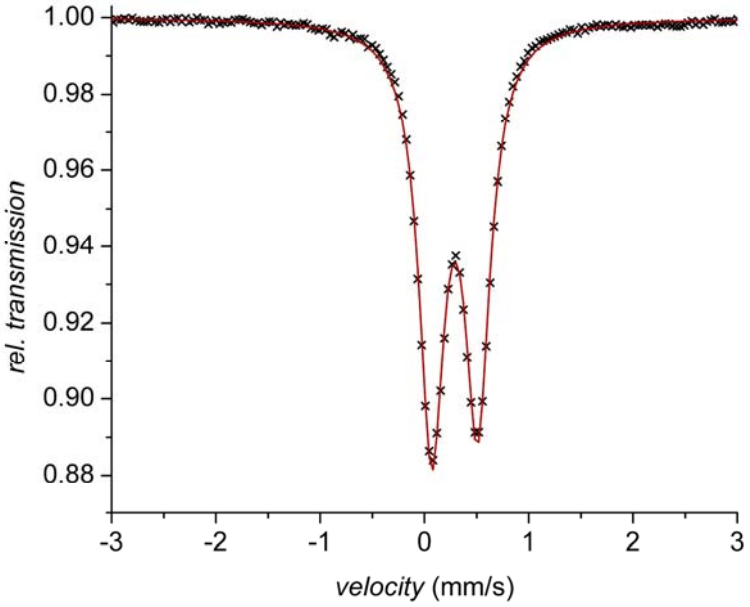

Figure S71: Zero-field Mössbauer spectrum of **4f** at 80 K, referenced to ^{57}Fe metal at room temperature. The solid lines are Lorentzian doublets fitted to the experimental values (crosses).

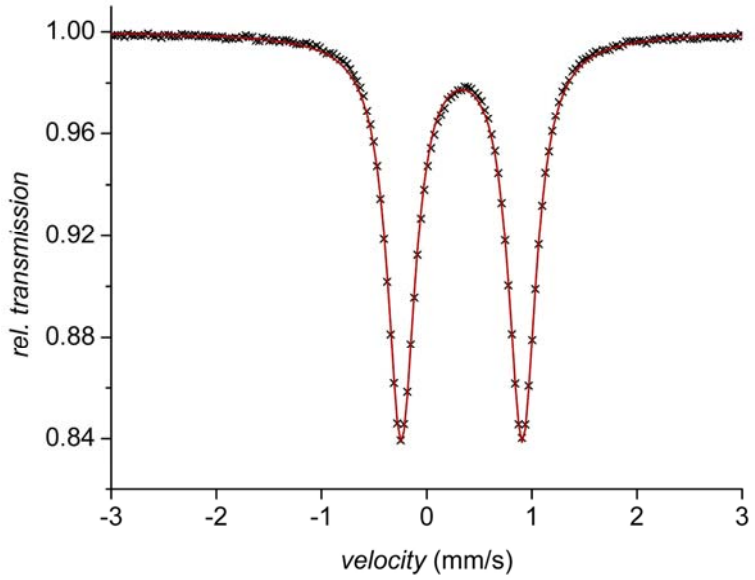

Figure S72: Zero-field Mössbauer spectrum of **5** at 80 K, referenced to ^{57}Fe metal at room temperature. The solid lines are Lorentzian doublets fitted to the experimental values (crosses).

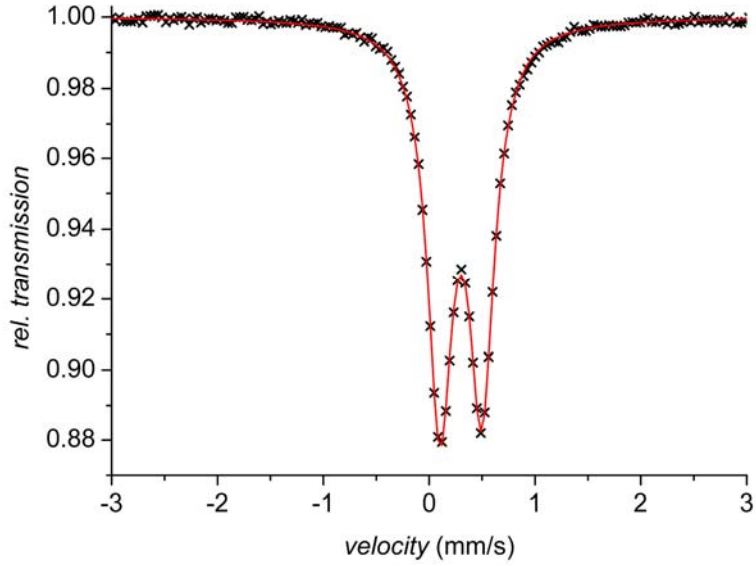

Figure S73: Zero-field Mössbauer spectrum of **6** at 80 K, referenced to ^{57}Fe metal at room temperature. The solid lines are Lorentzian doublets fitted to the experimental values (crosses).

8. Additional ORTEP plots

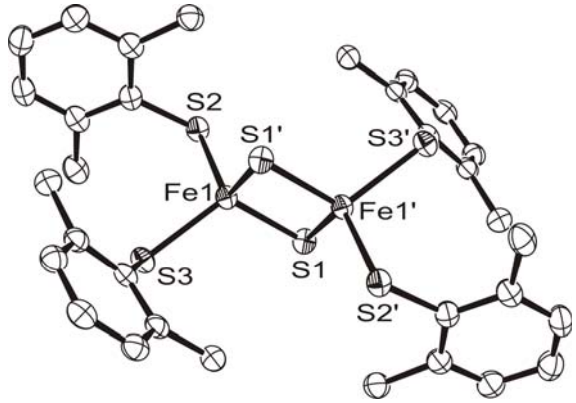

Figure S74: ORTEP plots (50% probability thermal ellipsoids) of the molecular structures of the dianions of **4c**. All hydrogen atoms have been omitted for clarity.

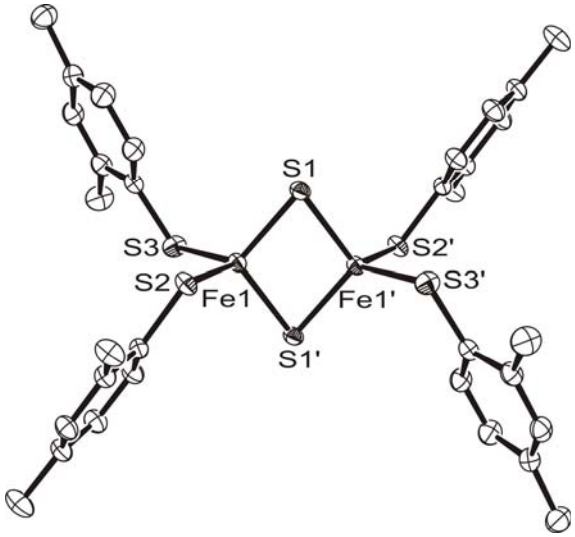

Figure S75: ORTEP plots (50% probability thermal ellipsoids) of the molecular structures of the dianions of **4e**. All hydrogen atoms have been omitted for clarity.